

Supplementary Information (SI) for Energy & Environmental Science.

This journal is © The Royal Society of Chemistry 2025

Supplementary Information

Reducing Energy Loss by Developing Luminescent Triphenylamine Functionalized Electron Acceptor for High- Performance Organic Solar Cells

*Yue Chen^{+a,b}, Xiaopeng Duan^{+a}, Junjie Zhang^b, Zhongwei Ge^b, Haisheng Ma^a, Xiaobo Sun^{*a,b}, Huotian Zhang^{*c}, Jiaxin Gao^d, Xuelin Wang^d, Xunchang Wang^e, Zheng Tang^d, Renqiang Yang^e, Feng Gao^c, and Yanming Sun^{*}*

^aHangzhou International Innovation Institute, Beihang University, 311115 Hangzhou, P. R. China

E-mail: sunxb@buaa.edu.cn; sunym@buaa.edu.cn

^bSchool of Chemistry, Beihang University, Beijing 100191, P. R. China

^cDepartment of Physics Chemistry and Biology (IFM), Linköping University, Linköping 58183, Sweden

E-mail: huotian.zhang@liu.se

^dState Key Laboratory for Modification of Chemical Fibers and Polymer Materials, Center for Advanced Low-dimension Materials, College of Materials Science and Engineering, Donghua University, Shanghai 201620, P. R. China

^eKey Laboratory of Flexible Optoelectronic Materials and Technology (Ministry of Education), School of Optoelectronic Materials & Technology, Jiangnan University, Wuhan 430056, P. R. China

⁺ These authors contributed equally: Yue Chen, Xiaopeng Duan

1. Experiment section

1.1 Materials

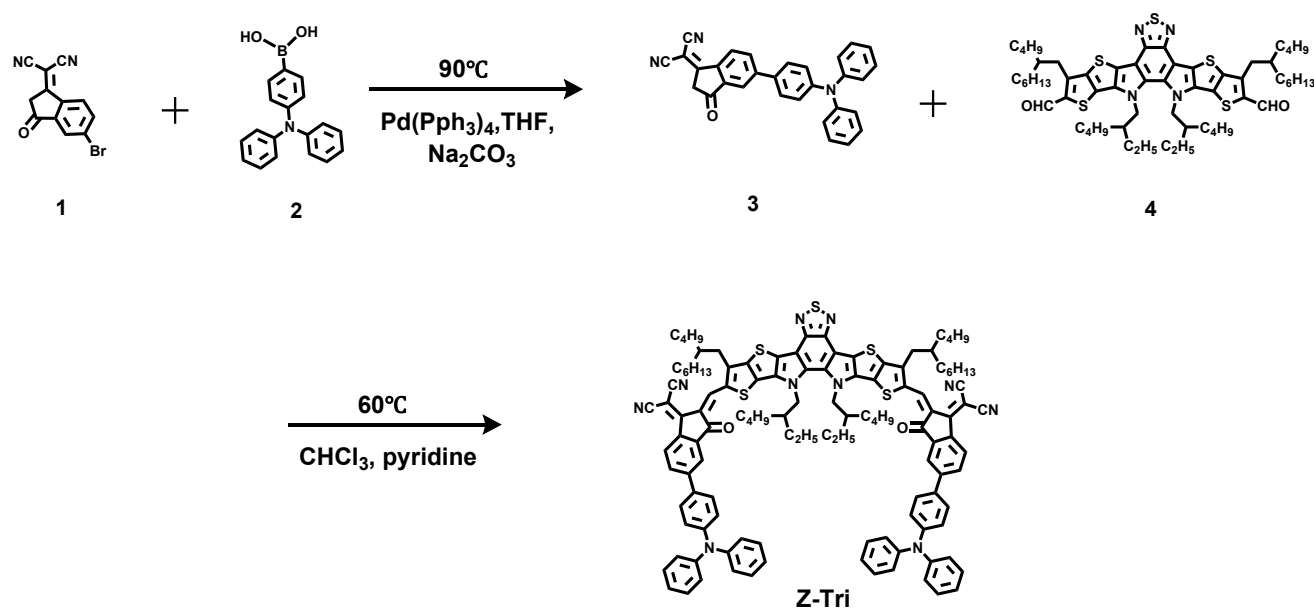
PM6 was purchased from Solarmer Materials (Beijing, China). Compound 1(2-(5-bromo-3-oxo-2,3-dihydro-1H-inden-1-ylidene) malononitrile) was purchased from Hyper Chemical Company. L8-BO and L8-BO-CHO (3,9-bis(2-butyloctyl)-12,13-bis(2-ethylhexyl)-12,13-dihydro-[1,2,5]thiadiazolo[3,4-e]thieno[2'',3'':4',5']thieno[2',3':4,5]pyrrolo[3,2-g]thieno[2',3':4,5]thieno[3,2-b]indole-2,10-dicarbald-ehyde) were meticulously prepared according to established literature methods.^[1] 1,3-dibromo-5-chlorobenzene (DBC1) was purchased from Leyan.com. Compound 2(4-(Diphenylamine)phenylboronic acid) and Pd(Pph₃)₄ were purchased from Energy Chemical. [2-(9H-Carbazol-9-yl)ethyl] phosphonic acid (2PACz) was purchased from Aladdin. All purchased materials were used without further purification. The detailed synthetic procedures and characterizations of the Z-Tri were described in the following sections.

1.2 Synthesis of Z-Tri

Compound 3: Compound 1 (273 mg, 1.00 mmol) and compound 2 (1446 mg, 5.00 mmol) were dissolved into tetrahydrofuran (45 ml) in a three-neck flask. K₂CO₃ (484 mg, 3.50 mmol) dissolved in water (6 ml) was added to the three-neck flask. The solution was flushed with nitrogen for 10 min. Then, add Pd (Pph₃)₄ (110 mg) to the solution, then let the solution temperature to 95°C for 5 h. Washed with saturated salt water and ethyl acetate. The solvent was removed under reduced pressure. The crude product was subsequently purified by column chromatography on silica gel to afford compound 3 as an orange solid (417 mg, 93% yield). ¹H NMR (500 MHz, CD₂Cl₂) δ 8.63 (d, *J* = 8.3 Hz, 1H), 8.19 – 8.00 (m, 2H), 7.60 (d, *J* = 8.8 Hz, 2H), 7.33 (dd, *J* = 8.5, 7.3 Hz, 4H), 7.22 – 7.07 (m, 8H), 3.72 (s, 2H).

Z-Tri: Compound 4 (L8-BO-CHO, 120 mg, 0.113 mmol) and compound 3 (396 mg, 0.904 mmol) were dissolved into dry chloroform (40 mL) in a three-neck flask. The solution was flushed with nitrogen for 15 min. After 0.6 mL pyridine was added, the mixture was stirred at 65°C overnight. After cooling to room temperature, the reaction mixture was poured into water and extracted several times with chloroform. Then the solvent was removed under reduced pressure, and the crude product was

purified by column chromatography on silica gel to yield Z-Tri as a black solid (187 mg, 87% yield). ^1H NMR (400 MHz, Chloroform- d) δ 9.15 (s, 2H), 8.73 (d, J = 8.4 Hz, 2H), 8.14 (d, J = 1.8 Hz, 2H), 7.97 (dd, J = 8.4, 1.9 Hz, 2H), 7.61 (d, J = 8.8 Hz, 4H), 7.34 (t, J = 8.5 Hz, 8H), 7.19 (m, 10H), 7.16 – 7.10 (m, 4H), 4.78 (t, J = 7.8 Hz, 2H), 3.19 (d, J = 7.5 Hz, 2H), 2.11 (m, 4H), 1.39 (m, 4H), 1.24 (m, 32H), 1.03 (m, 10H), 0.85 (dt, J = 13.8, 6.9 Hz, 12H), 0.76 (td, J = 7.5, 3.8 Hz, 6H), 0.64 (td, J = 7.2, 4.0 Hz, 6H); ^{13}C NMR (126 MHz, CDCl_3 , δ): 188.49, 160.60, 152.31, 149.18, 147.60, 147.09, 146.45, 144.94, 137.99, 137.76, 137.74, 134.96, 134.09, 133.54, 132.23, 131.02, 129.70, 129.57, 127.92, 125.64, 125.33, 123.97, 122.48, 121.58, 120.26, 115.90, 115.39, 113.35, 67.22, 55.73, 40.35, 39.85, 34.52, 33.56, 33.30, 31.84, 29.73, 29.66, 28.87, 28.85, 27.67, 26.61, 26.59, 23.36, 23.33, 23.01, 22.88, 22.86, 22.67, 14.11, 14.07, 13.79, 13.77, 10.40; MS (MALDI-TOF) m/z : $[\text{M} + \text{H}]^+$ calcd for $\text{C}_{120}\text{H}_{120}\text{N}_{10}\text{O}_2\text{S}_5$, 1892.82, found: 1892.97.



Scheme S1. Synthetic routes of Z-Tri.

1.3 Device fabrication

All the OSCs devices were fabricated by using a conventional structure of ITO/2PACz/active layer/PNDIT-F3N/Ag. The ITO-coated substrates were sequentially cleaned by detergent deionized water, acetone, and isopropyl alcohol for 20 min in an ultrasonic cleaning machine. The cleaned ITO-

coated substrates were dried in an oven at 100 °C overnight. Before use, the ITO-coated substrates were pretreated by a plasma cleaner for 1 min under a vacuum condition below 10 Pa. Then a monolayer of 2PACz (0.3 mg mL⁻¹ in ethanol) was firstly deposited on the top of the ITO substrates at a rate of 3000 rpm for 30 s, followed by thermal annealing at 100 °C for 10 min under ambient conditions. The PM6:L8-BO (1:1.2 w/w) was dissolved in chloroform at the donor concentration of 7.3mg/mL with 165 wt% DBCl as the solid additive. The PM6:Z-Tri (1:1.2 w/w) was dissolved in chloroform at the donor concentration of 7.3mg/mL with 165 wt% DBCl as the solid additive. The PM6:L8-BO: Z-Tri (1:1:0.2 w/w/w) was dissolved in chloroform at the donor concentration of 7.3mg/mL with 165 wt% DBCl as the solid additive. Then the active layers with different amounts of Z-Tri were spin-cast on the 2PACz layer surface in an N₂-filled glove box at 2800 rpm for 40 s with a total concentration of 16 mg mL⁻¹ in chloroform (CF). The active layer solutions were stirred at 80 °C for 4h before used. Then, the active layers were thermally annealed at 80 °C for 8 min. Subsequently, a thin layer of PNDIT-F3N (1.2 mg mL⁻¹ in methanol with 0.5% acetic acid, v/v) was spin-coated onto the active layer at a rate of 4200 rpm for 30 s. Finally, a 120 nm-thick silver layer was thermally deposited under a vacuum condition of 2×10⁻⁴ Pa. The active area of devices is 5.12 mm².

1.4 Device characterization

***J-V* and EQE Measurements**

The devices were tested through a mask with an area of 3.15 mm². The device performance was measured by using a 510 Air Mass 1.5 Global (AM1.5G) solar simulator (SS-F5-3A, Enlitech) with an irradiation intensity of 100 mW cm⁻², which was determined by using a calibrated silicon solar cell (SRC2020, Enlitech). The *J-V* characteristics were measured by using a Keithley 2400 Source Measure Unit. EQE spectra were performed by using a QE-R3011 Solar Cell EQE measurement system (Enlitech).

Time-dependent density functional theory (TD-DFT) calculations

All calculations were optimized using the ORCA 5.0.4 program package. The R2SCAN-3c composite method proposed by S.Grimme was used to optimize the structure and ωB97X-D3 hybrid functional combined with Def2-TZVP was used for single point calculations. The solvent effect of chloroform

was considered, using the continuum polarizable continuum model (CPCM). All post-calculation analysis was carried out using the Multiwfn 3.8.4 Dev software package and the results were visualized using visual molecular dynamics (VMD) 1.8.4. .

Ultraviolet-visible (UV-vis) spectroscopy measurements

UV-vis absorption spectra of the pristine and blend films were acquired with a UV-vis spectrophotometer (Shimadzu UV-3600).

Cyclic Voltammogram (CV) Measurements

Cyclic voltammogram (CV) measurement was carried out on a CHI660E electrochemical workstation with three electrodes, employing glassy carbon discs as the working electrode, Pt wire as the counter electrode, and Ag/AgCl electrode as the reference electrode at a scanning rate of 100 mV s⁻¹ under a nitrogen atmosphere. Tetrabutylammonium hexafluorophosphate (Bu₄NPF₆, 0.1 mol/L) dissolved in acetonitrile (HPLC grade) was adopted as the supporting electrolyte. PBDF-NS was drop-cast the electrode from chloroform solutions to form thin films. Potentials were referenced to the ferrocene/ferrocenium (Fc/Fc⁺) redox couple by using ferrocene as the external standard in acetonitrile solutions ($E_{\text{Fc}/\text{Fc}^+}=0.42$ eV). $E_{\text{HOMO}}=-[(4.8-E_{\text{Fc}/\text{Fc}^+})+E_{\text{ox}}]$ (eV); $E_{\text{LUMO}}=-[(4.8-E_{\text{Fc}/\text{Fc}^+})+E_{\text{red}}]$ (eV).

Space-charge-limit current (SCLC)

The SCLC method was used to study the charge transport properties of neat film and blend films. The hole-only and electron-only devices were fabricated with a structure of ITO/2PACz/PM6:NFA/MoO₃/Ag and ITO/ZnO/PM6:NFA/PNDIT-F3N/Ag, respectively. The charge carrier mobility was determined by fitting the corresponding J - V characteristics by using the equation of $J=9\varepsilon_0\varepsilon_r\mu V^2/8L^3$, where J is the current density, ε_0 is the permittivity of free space, ε_r is the permittivity of the active layer, μ is the charge carrier mobility (μ_h and μ_e), V is the effective voltage ($V=V_{\text{appl}}-V_{\text{bi}}-V_{\text{R}}$, in which V_{appl} is the applied voltage, V_{bi} is the built-in potential and V_{R} is the voltage loss from series resistance of the device) and L is the film thickness of the neat film or blend film.

Steady state photoluminescence (PL) measurements

PL spectra were collected by a spectrometer (DU420A-OE, ANDOR). Fluorescence decay dynamics were recorded by TCSPC (Becker&Hickl, SPC-150).

sEQE measurements.

The sEQE measurements were conducted using a halogen lamp light source, a monochromator (Newport CS260), a Stanford SR830 lock-in amplifier, and a Stanford SR570 current amplifier. The lamp intensity was calibrated by a Si detector (Hamamatsu s1337-1010BQ).

EL measurements

The EL spectra were measured by using a source meter (Keithley 2400) to inject electric current, and recorded by a Kymera-328I spectrograph and a Si EMCCD purchased from Andor Technology (DU970P), and a InGaAs CCD camera (DU491A-1.7, Andor Technology).

EQE_{EL} measurements

EQE_{EL} was determined by a homebuilt setup using a Keithley 2400 to inject current into the solar cells. The Si detector (Hamamatsu s1337-1010BQ) and a Keithley 6482 picoammeter were used to determine the emission photon-flux of the solar cells.

Contact angle measurements

The water and glycerol contact angle images of neat films were recorded by using a KRÜSS DSA 100 instrument under atmospheric condition.

Grazing Incidence Wide-Angle X-ray Scattering (GIWAXS)

GIWAXS measurements were conducted at beamline 7.3.3 of the Advanced Light Source. Samples were prepared on Si substrates utilizing blend solutions identical to those employed in the fabrication of devices. A 10 keV X-ray beam was incident at a grazing angle ranging from 0.12° to 0.16°, chosen to optimize the scattering intensity from the samples. The scattered X-rays were captured by a Dectris Pilatus 2M photon counting detector.

Atomic Force Microscopy (AFM) measurement

AFM measurement was performed on a Dimension Icon AFM (Bruker) in a tapping mode under ambient conditions. (GIWAXS) patterns were acquired by detector Pilatus3R 1M, Dectris (X-ray Source: MetalJet-D2, Excillum).

Photo-induced Force Microscopy (PiFM)

PiFM is a multimodal Atomic Force Microscopy (AFM) technique that integrates the high resolution of AFM with infrared spectroscopy to acquire topographical and molecular information with sub-10 nanometer resolution. All measurements were conducted using Molecular Vista's Visascope microscope and Block Engineering's Laser Tune QCL, with an adjustable range from 775 to 1885 cm^{-1} and a spectral linewidth of 2 cm^{-1} . PiFM images were created with a resolution of 256×256 pixels, line speed of 0.89 lines/s, and a size of 1 μm^2 , using wavenumbers 1648 cm^{-1} , 1278 cm^{-1} , and 1539 cm^{-1} to emphasize the PM6, L8-BO, and Z-Tri.

Transient absorption spectroscopy (TAS) measurement

Femtosecond transient absorption spectroscopy measurements were performed on an Ultrafast Helios pump-probe system in collaboration with a regenerative amplified laser system from Coherent. An 800 nm pulse with a repetition rate of 1kHz, a length of 100 fs, and an energy of 7 mJ/pulse, was generated by an Ti:sapphire amplifier (Astrella, Coherent). The time delay between pump and probe was controlled by a motorized optical delay line with a maximum delay time of 8 ns. The samples films were spin-coated onto the 1 mm-thick quartz plates and are encapsulated by epoxy resin in nitrogen-filled glove box to resist water and oxygen in the air. The pump pulse is chopped by a mechanical chopper with 500 Hz and then focused on to the mounted sample with probe beams. The probe beam was collimated and focused into a fiber-coupled multichannel spectrometer with CCD sensor. The energy of pump pulse was measured and calibrated by a power meter (PM400, Thorlabs)

Estimation of glass-transition temperature (T_g)

The glass transition temperature (T_g) was determined using ultraviolet-visible spectroscopy. Absorption spectra measurements were conducted on the receptor thin film, with the annealing temperature ranging from 20°C to 240°C. Then, the deviation metric (DMT) of the each absorption spectra was calculated, following the method from Samuel E. Root et al. $DMT = \sum_{\lambda_{\min}}^{\lambda_{\max}} [I_{RT}(\lambda) - I_T(\lambda)]^2$ where λ is the wavelength, λ_{\max} and λ_{\min} are the upper and lower bounds of the optical sweep, respectively, $I_{RT}(\lambda)$ and $I_T(\lambda)$ are the normalized absorption intensities of the as-cast (room temperature) and annealed films, respectively. Then, T_{g_s} were determined to points where the two interpolated lines in low- and high-temperature regions intersect.

2. Figures and Tables

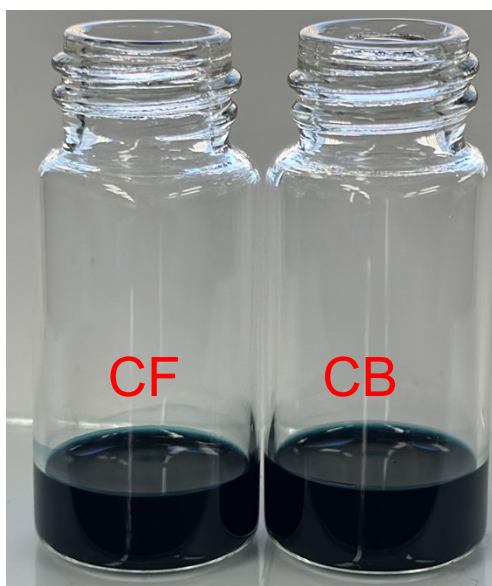


Fig. S1. Photograph of Z-Tri dissolved in chloroform and chlorobenzene solutions.

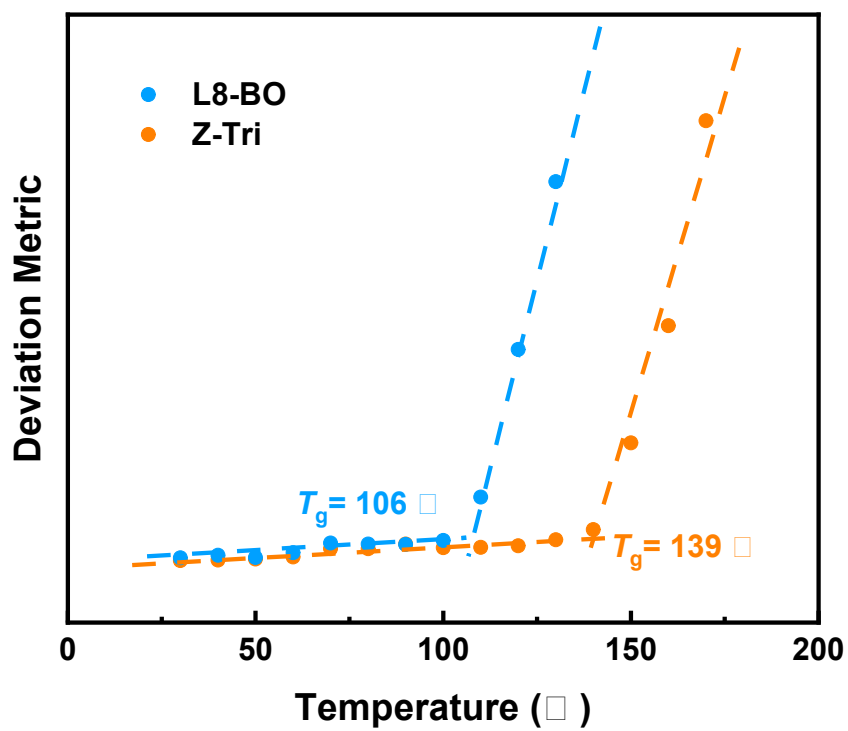


Fig. S2. UV-Vis deviation metric results of L8-BO and Z-Tri.

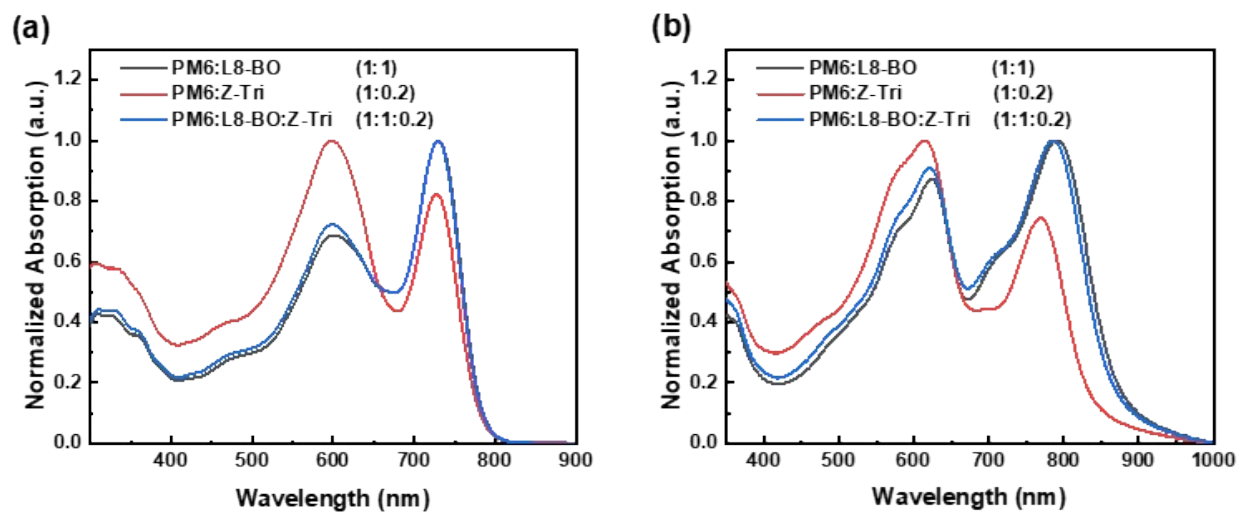


Fig. S3. UV-vis absorption spectra of blend films (a) in the solutions and (b) in the films.

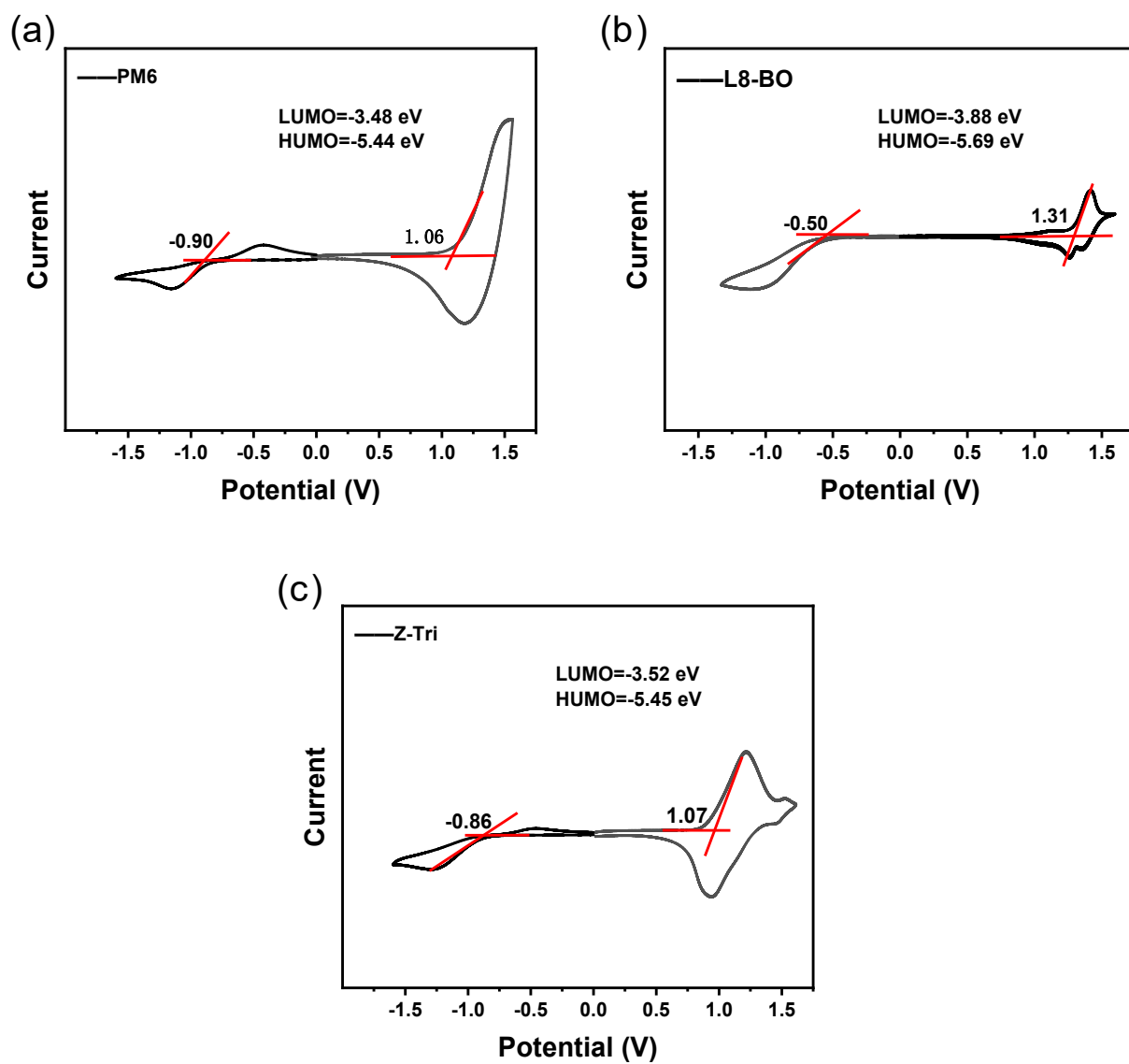


Fig. S4. Cyclic voltammetry curves of (a) PM6, (b) L8-BO, and (c) Z-Tri.

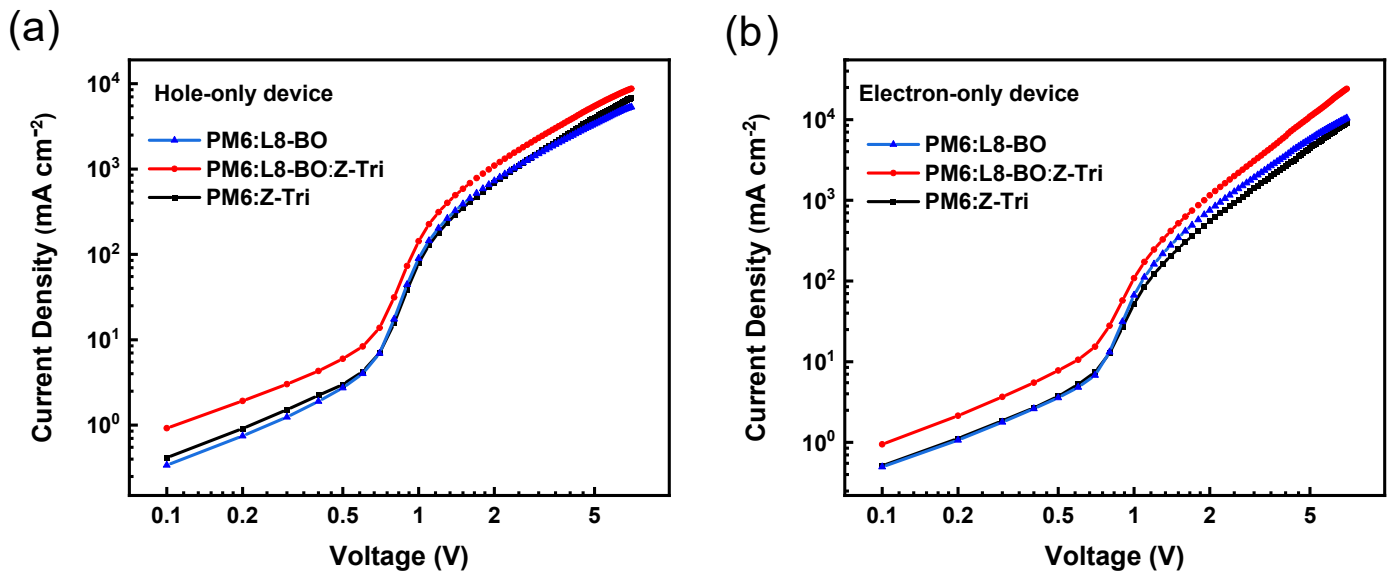


Fig. S5. (a) SCLC curves of hole-only devices based on binary and ternary devices. (b) SCLC curves of electron-only devices based on binary and ternary devices.

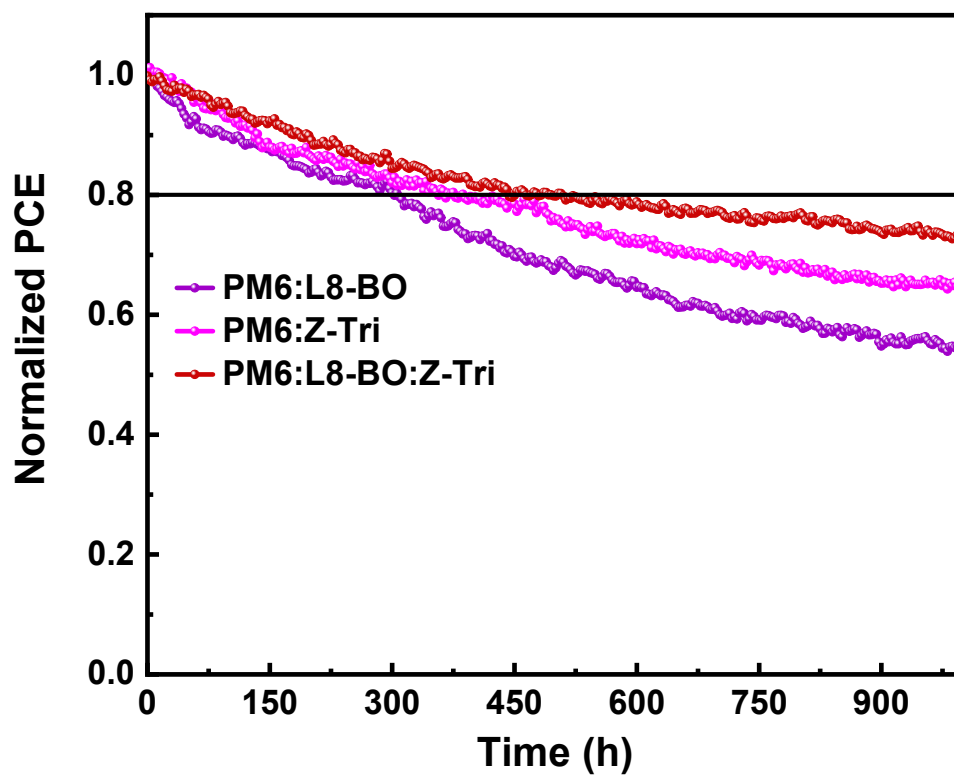


Figure S6. The photostability of the solar cells under continuous 100 mW/cm² illumination in air.

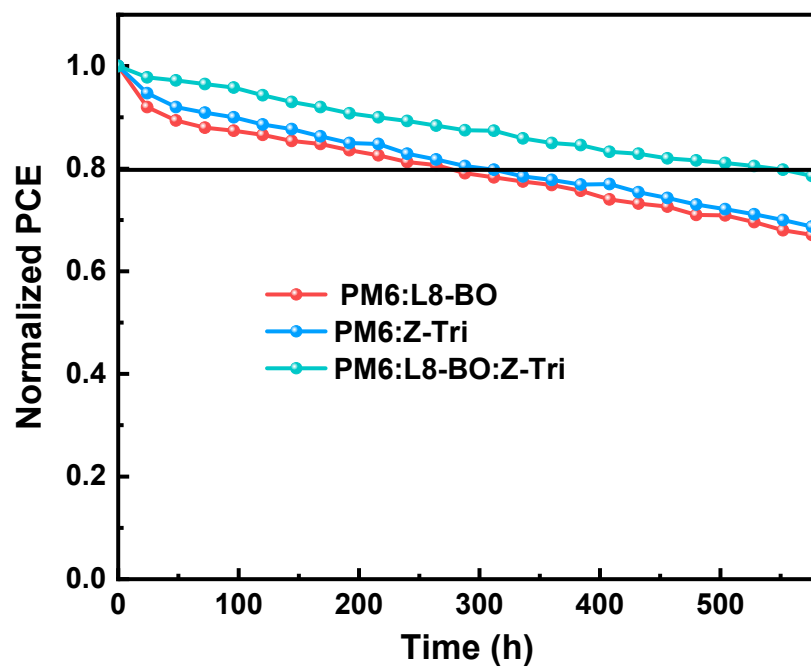


Figure S7. The thermal stability of the solar cells under continuous heating at 80°C.

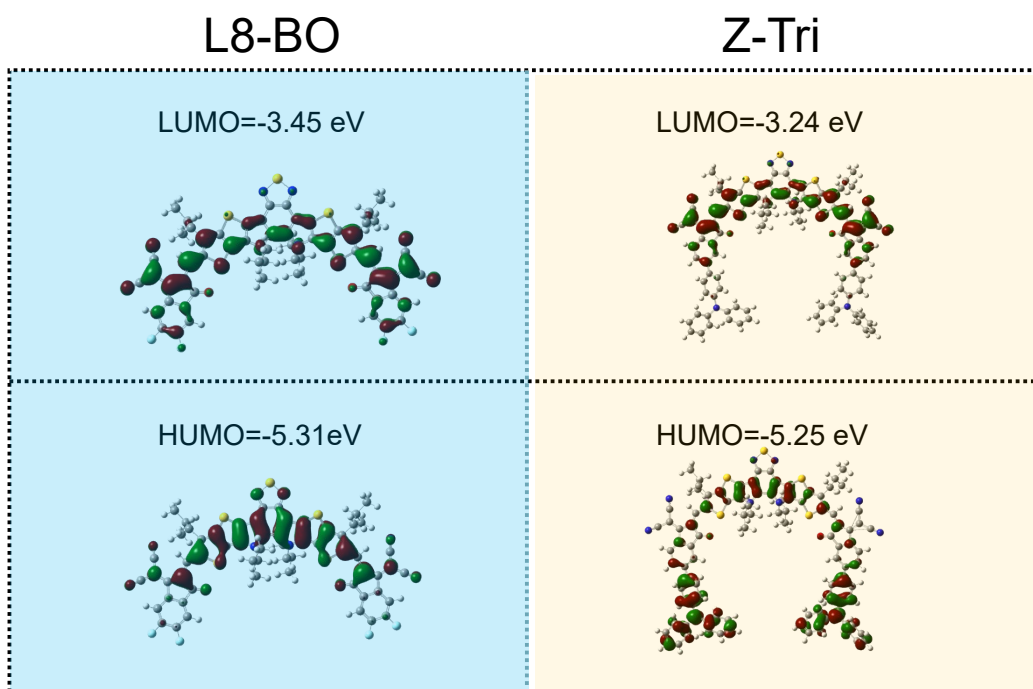


Fig. S8. The HOMO/LUMO structures of L8-BO and Z-Tri are based on DFT (B3LYP/6-31G level) calculation. (Alkyl side chains were replaced with methyl groups for simplifying calculation.)

Heat Maps Calculation

In the donor-acceptor (D-A) interface of OSCs, heat maps are crucial for demonstrating the charge transfer process. They vividly display the electron transfer from the donor to the acceptor and the hole accumulation in the donor. On the heat map, the electron concentration gradually increases on the acceptor side, indicating successful electron migration from the donor material, which is a key step in the charge-separation process of OSCs. Meanwhile, the hole concentration rises on the donor side as electrons leave, leaving behind holes that accumulate in this region. Such visualization by heat maps directly reflects the charge transfer direction. The movement of electrons and the corresponding hole accumulation define the charge-transfer pathway. Additionally, the degree of change in electron and hole concentrations on the heat map can be used to infer the charge transfer efficiency. A steeper increase in electron concentration on the acceptor side and a more significant rise in hole concentration on the donor side may imply a more efficient process, whereas a less pronounced change may suggest barriers or inefficiencies in the interface's charge-transfer mechanism. Overall, heat maps are powerful tools for understanding the charge-transfer behavior at the D-A interface, essential for improving device.

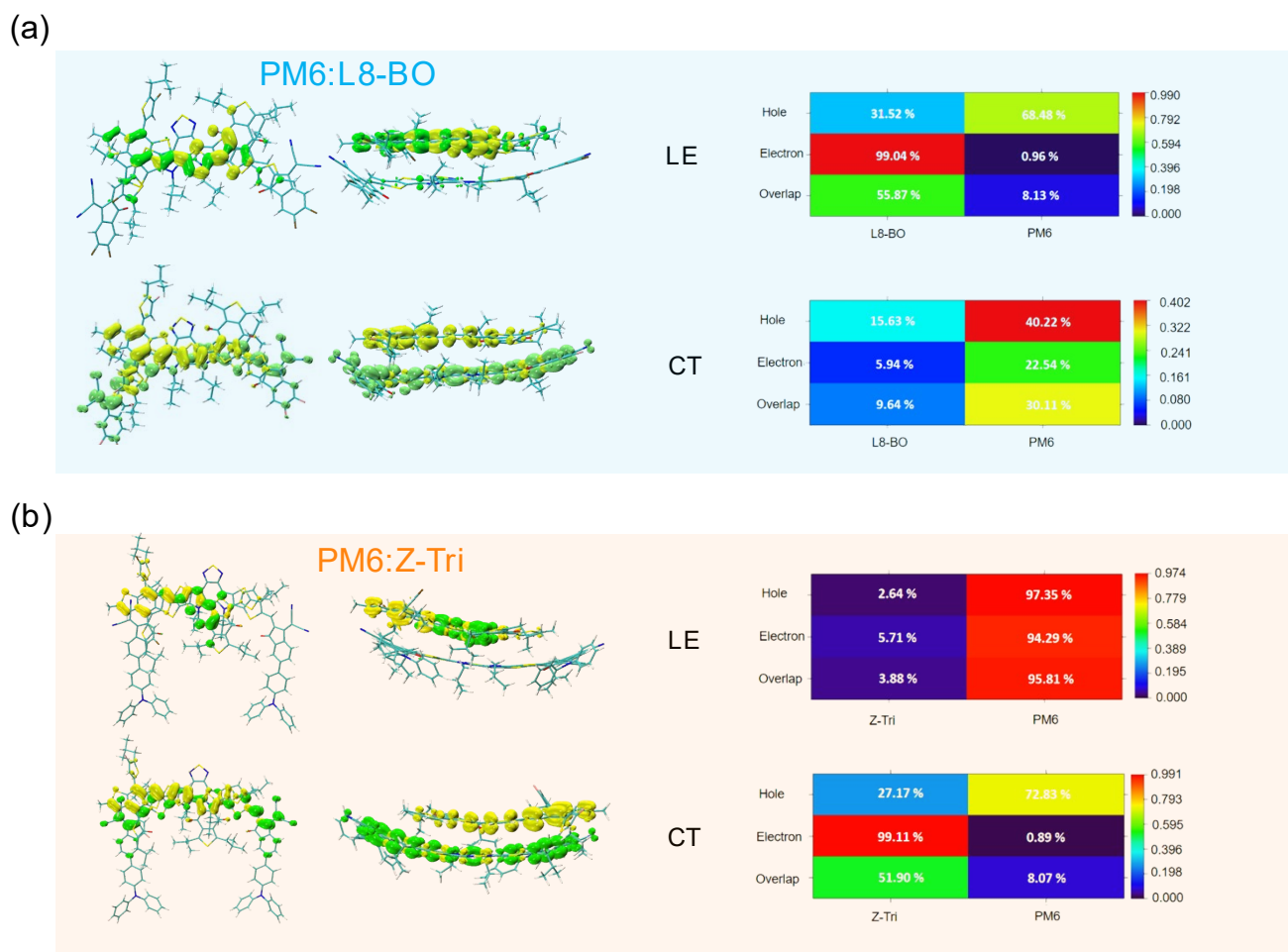


Fig. S9. Optimized geometry of the PM6:L8-BO and PM6:Z-Tri complexes, electron-hole distribution diagram.

Luminescence Lifetime Calculation

The formula for calculating the luminescence lifetime is expressed as:

$$\tau = \frac{1.5}{f \cdot \Delta E^2} \quad (1)$$

This formula plays a crucial role in the field of luminescence research, enabling us to quantitatively determine the duration for which a luminescent material emits light. In this formula, the variable τ represents the luminescence lifetime, and its unit is seconds. The luminescence lifetime is a key parameter that characterizes the decay behavior of the excited - state population in a luminescent system. It provides valuable information about the stability and efficiency of the luminescence process. On the other hand, ΔE is the energy gap. It is measured in the unit of cm^{-1} , which is a commonly used unit in spectroscopy to describe energy differences between energy levels. This energy gap is related to the electronic or vibrational transitions within the luminescent material. Based on the mathematical form of the formula 1, we can clearly observe an inverse - square relationship between the luminescence lifetime τ and the energy gap ΔE . As the value of the energy gap ΔE becomes smaller, the denominator $f \cdot \Delta E^2$ of the formula decreases. Since the numerator is a constant value of 1.5, a decrease in the denominator leads to an increase in the value of the entire fraction. Consequently, the luminescence lifetime τ becomes longer. This relationship is of great significance in understanding the fundamental mechanisms of luminescence and in the design and optimization of luminescent materials.

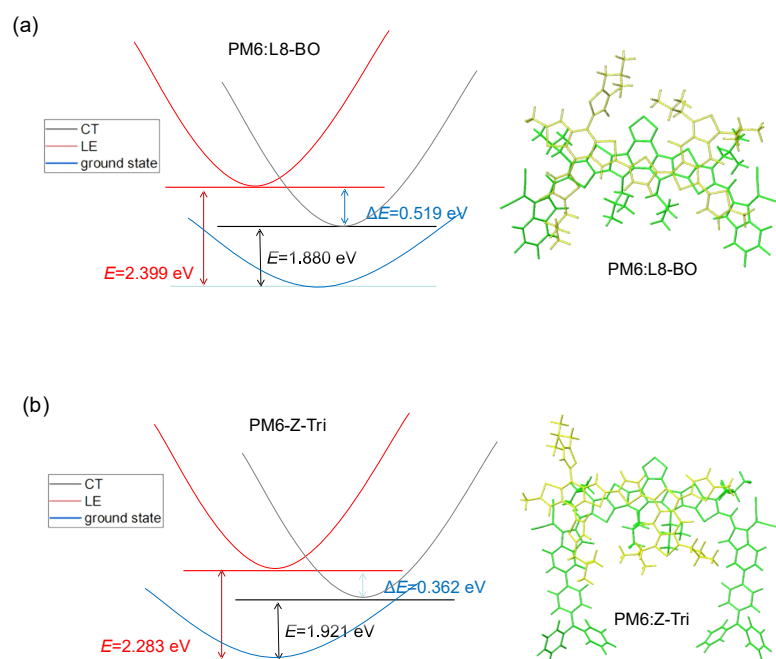


Fig. S10. Optimized geometry of the (a) PM6:L8-BO and (b) PM6:Z-Tri excitation process diagram, and diagram of corresponding energy states.

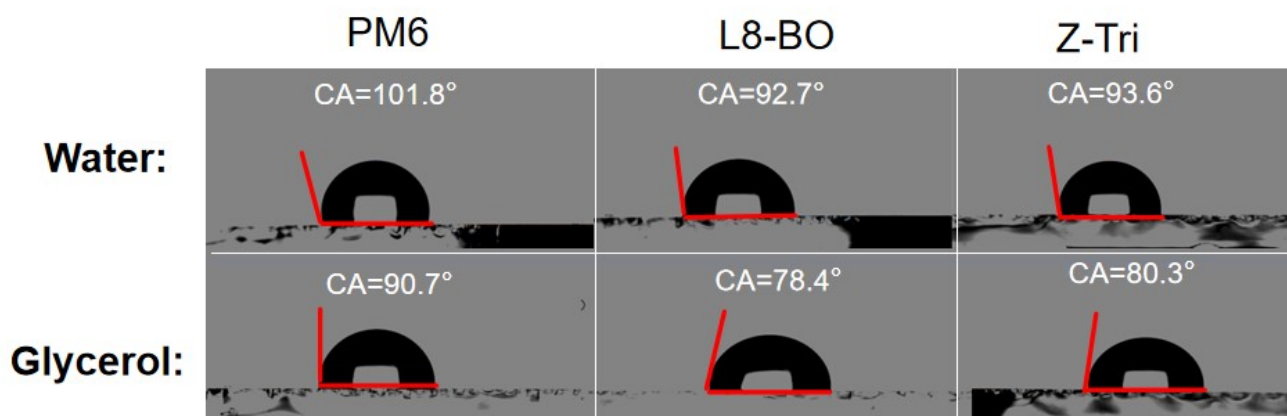


Fig. S11. Contact angles of PM6, L8-BO, and Z-Tri neat films based on water and glycerol drops.

Energy Loss Calculation

As shown in equation 2, E_{loss} can be segmented into three distinct components: the radiative recombination loss from absorption above the bandgap (ΔE_1), the additional radiative recombination loss from the absorption below the bandgap (ΔE_2), and the non-radiative recombination loss (ΔE_{nr}). ΔE_1 defined as $E_g - qV_{\text{oc}}^{\text{SQ}}$ ($qV_{\text{oc}}^{\text{SQ}}$ is maximum V_{oc} predicted by the Shockley–Queisser limit) strongly depends on the E_g , which is considered as unavoidable loss in any types of solar cells. ΔE_2 can be obtained from the equation of $qV_{\text{oc}}^{\text{SQ}} - qV_{\text{oc}}^{\text{rad}}$, where $V_{\text{oc}}^{\text{rad}}$ is V_{oc} when only considering radiative recombination. By fitting sEQE and EL spectra, we determined the $V_{\text{oc}}^{\text{rad}}$ of the device.

$$\begin{aligned}
 E_{\text{loss}} = E_g - qV_{\text{oc}} &= (E_g - qV_{\text{oc}}^{\text{SQ}}) + (qV_{\text{oc}}^{\text{SQ}} - qV_{\text{oc}}^{\text{rad}}) + (qV_{\text{oc}}^{\text{rad}} - qV_{\text{oc}}) \\
 &= (E_g - qV_{\text{oc}}^{\text{SQ}}) + (q\Delta V_{\text{oc}}^{\text{rad, belowgap}}) + (q\Delta V_{\text{oc}}^{\text{non-rad}}) \\
 &= \Delta E_1 + \Delta E_2 + \Delta E_{\text{nr}}
 \end{aligned} \tag{2}$$

ΔE_{nr} has been recognized as the key factor to limit the V_{oc} of OSCs, which can be calculated from the equation 3:

$$\Delta E_{\text{nr}} = -KT \ln(\text{EQEEL}) \tag{3}$$

where K is the Boltzmann constant, T is the Kelvin temperature. The E_g is determined by identifying the intersection points of EL and absorption spectra of the blend film.

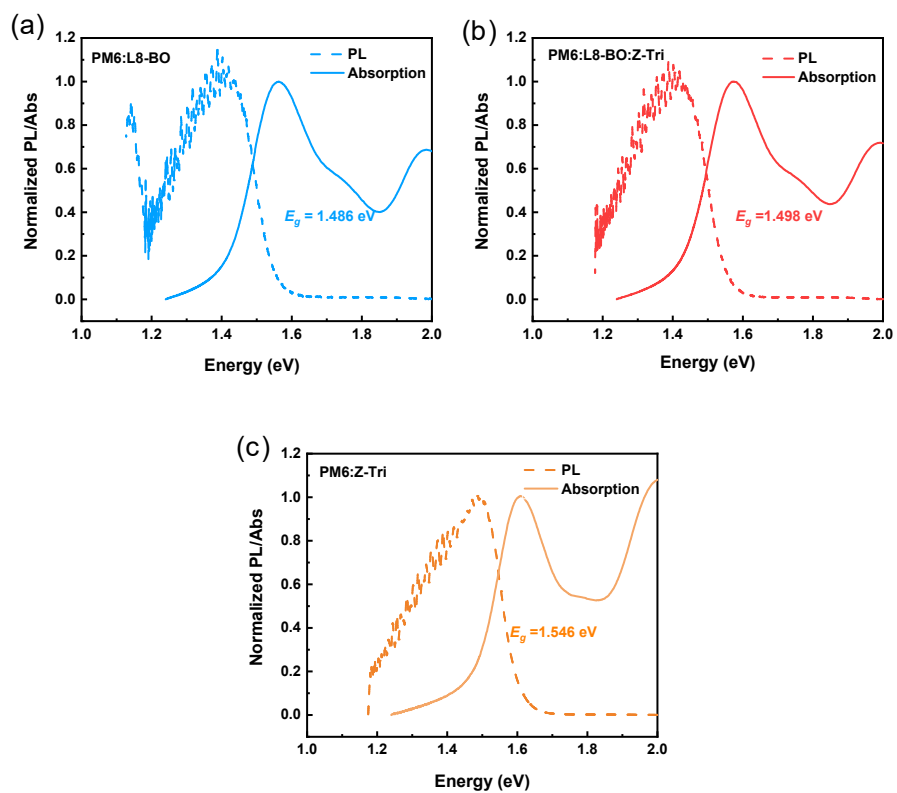


Fig. S12. Normalized reduced PL and absorption spectra of (a) PM6:L8-BO (b)PM6:L8-BO: Z-Tri, and (c) PM6: Z-Tri films.

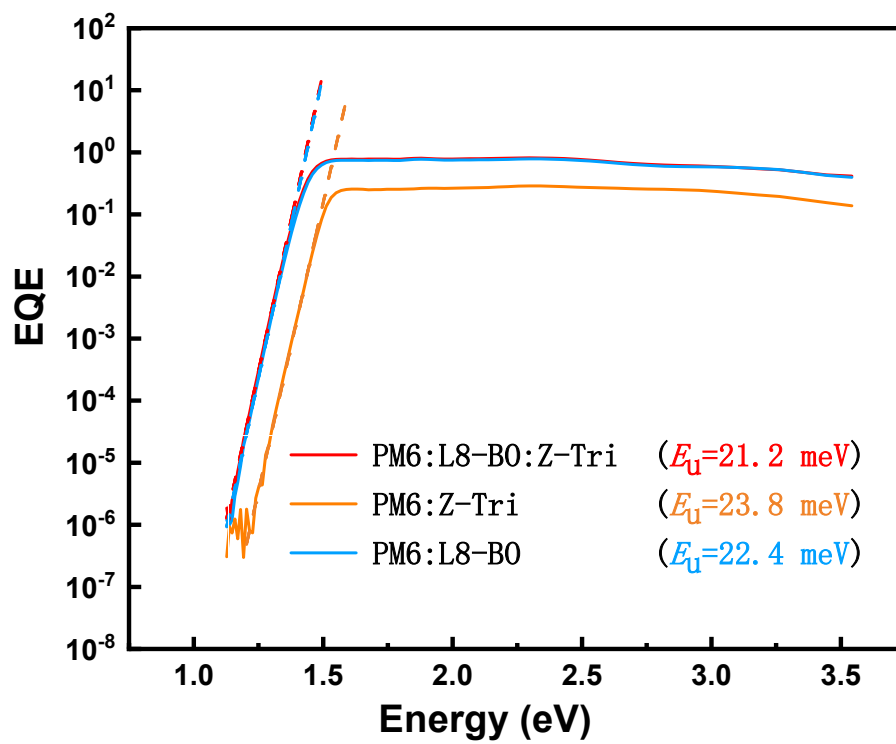


Fig. S13. EQE of the binary and ternary devices.

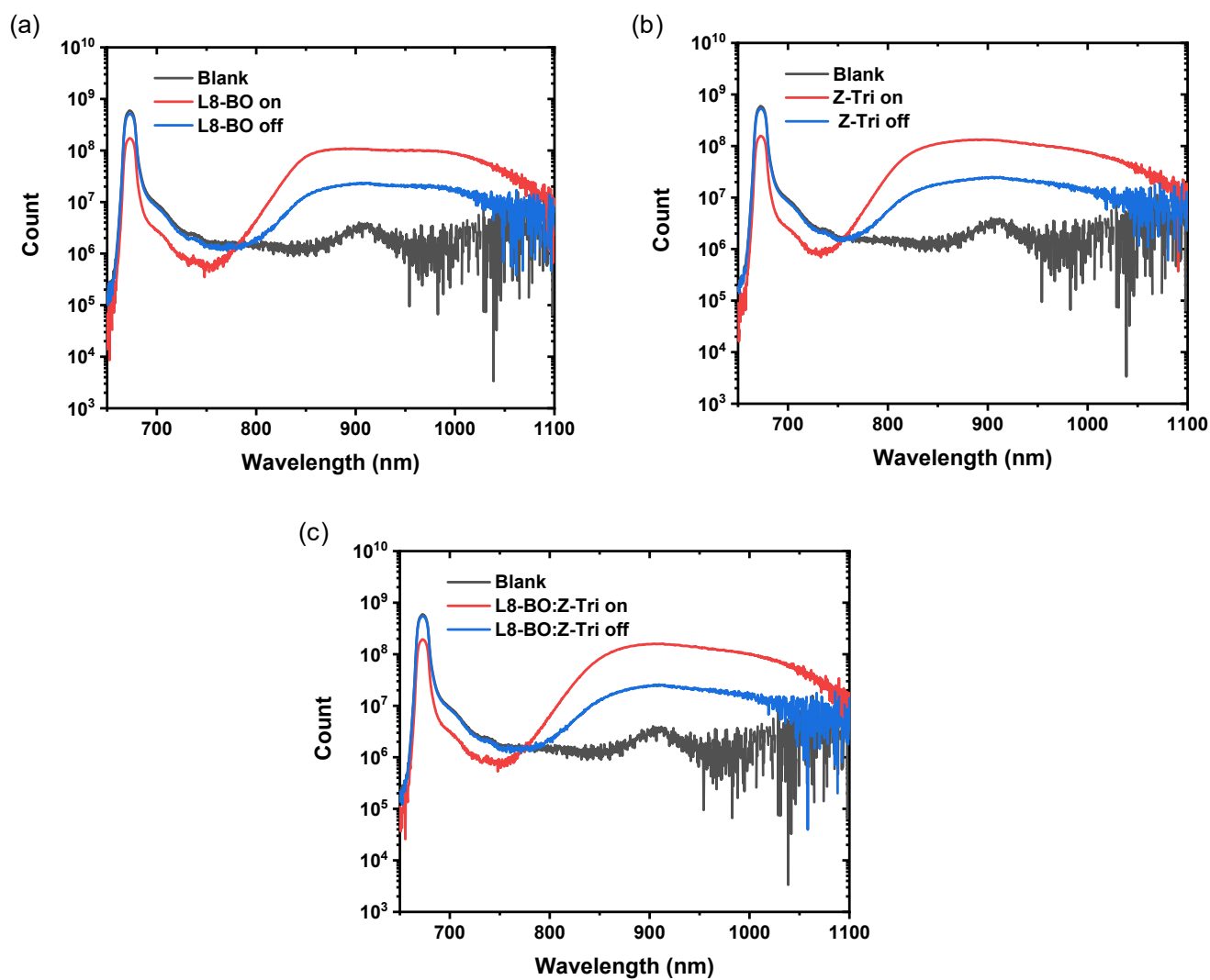


Fig. S14. Schematic for a PLQY measurement of (a) L8-BO, (b) Z-Tri, and (c) L8-BO:Z-Tri. (The red line is the light on the sample, directly exciting the sample, blank substrate beside; The blue line is the light hitting the blank substrate, scattering the light to excite the sample; The black lines are only two blank substrates inside the integrating sphere.)

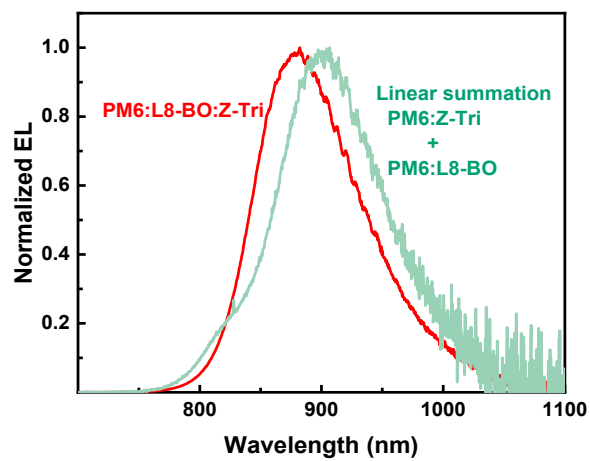


Fig. S15. The EL spectra of PM6:L8-BO:Z-Tri and binary blends (16.7% PM6:L8-BO+83.3% PM6:Z-Tri).

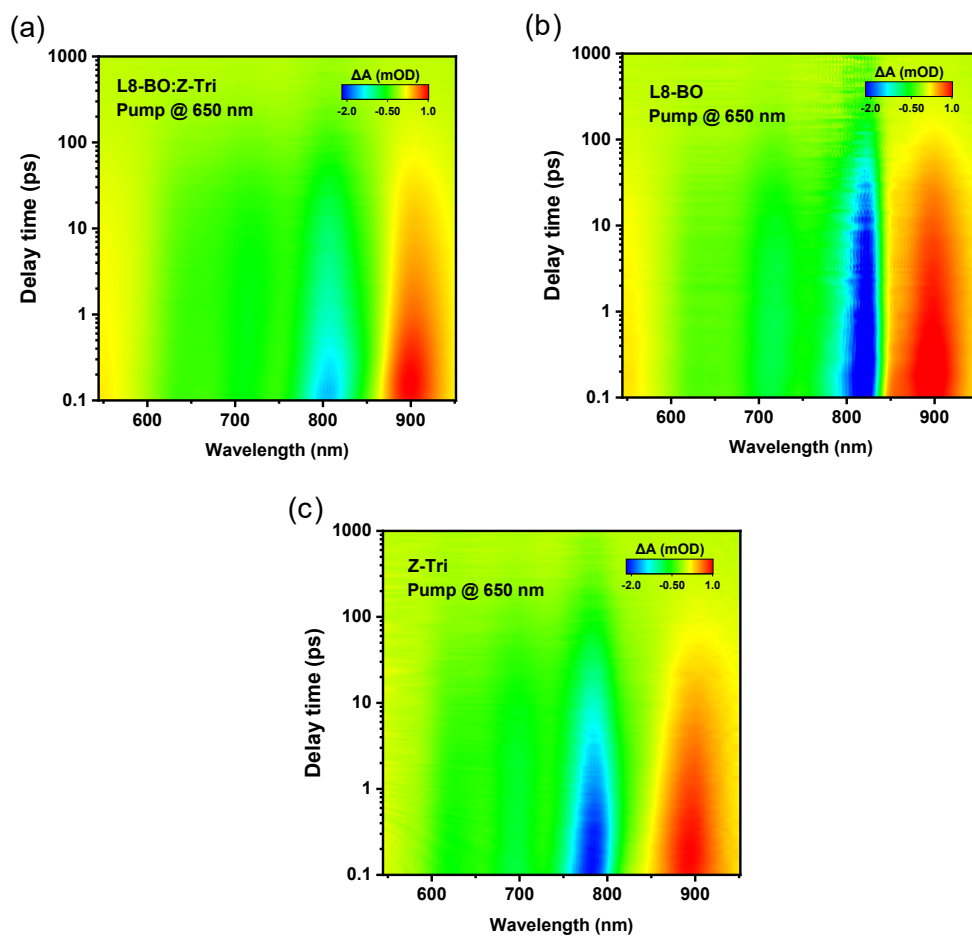


Fig. S16. 2D TAS images of (a) L8-BO:Z-Tri, (b) L8-BO, and (c) Z-Tri films with 650 nm excitation.

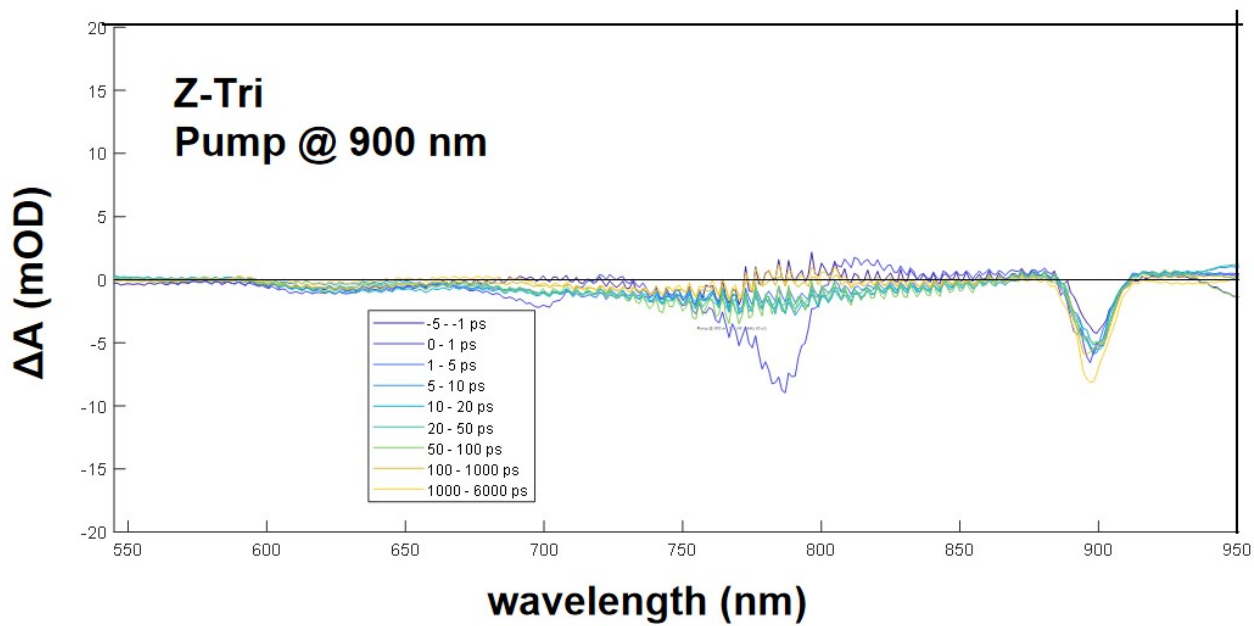


Fig. S17. TA spectra of the Z-Tri pumped at 900 nm.

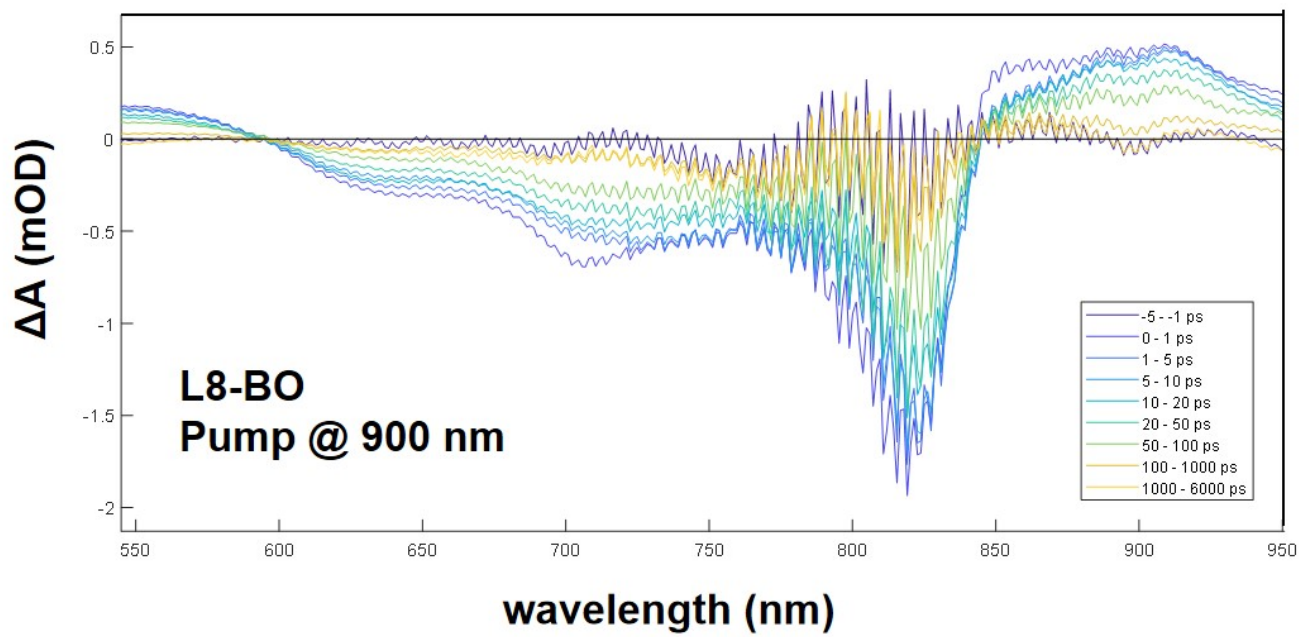


Fig. S18. TA spectra of the L8-BO pumped at 900 nm.

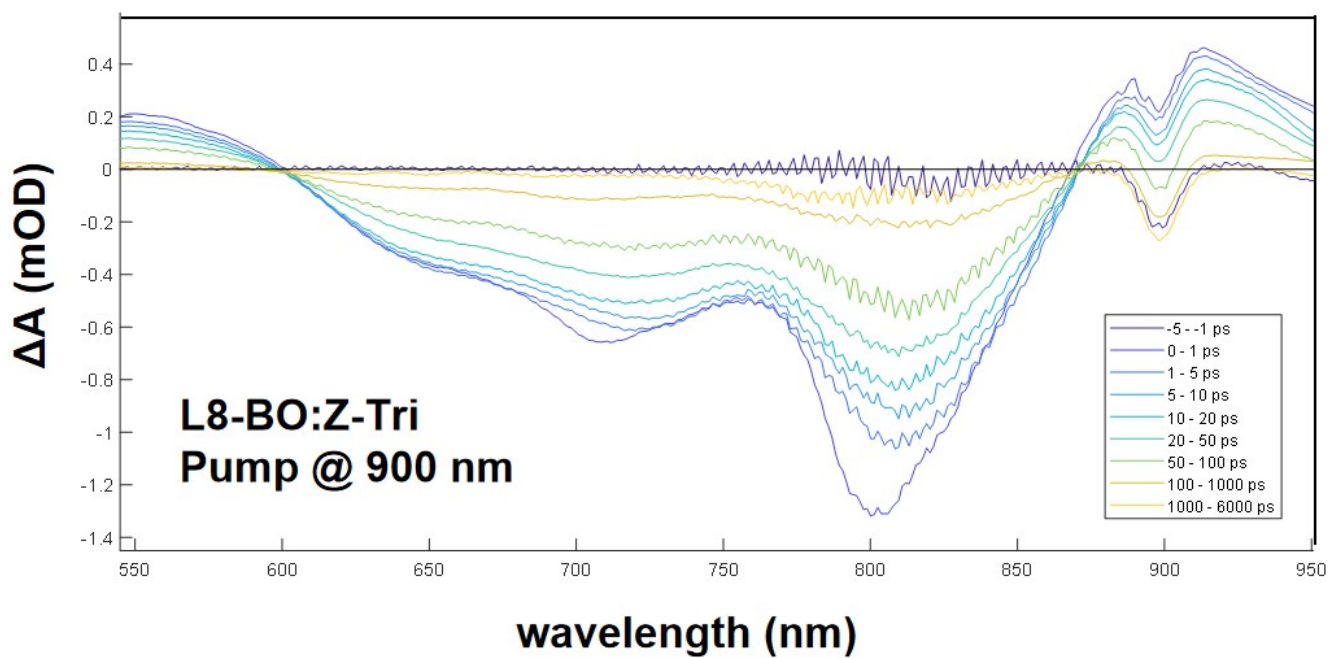


Fig. S19. TA spectra of the L8-BO:Z-Tri blends pumped at 900 nm.

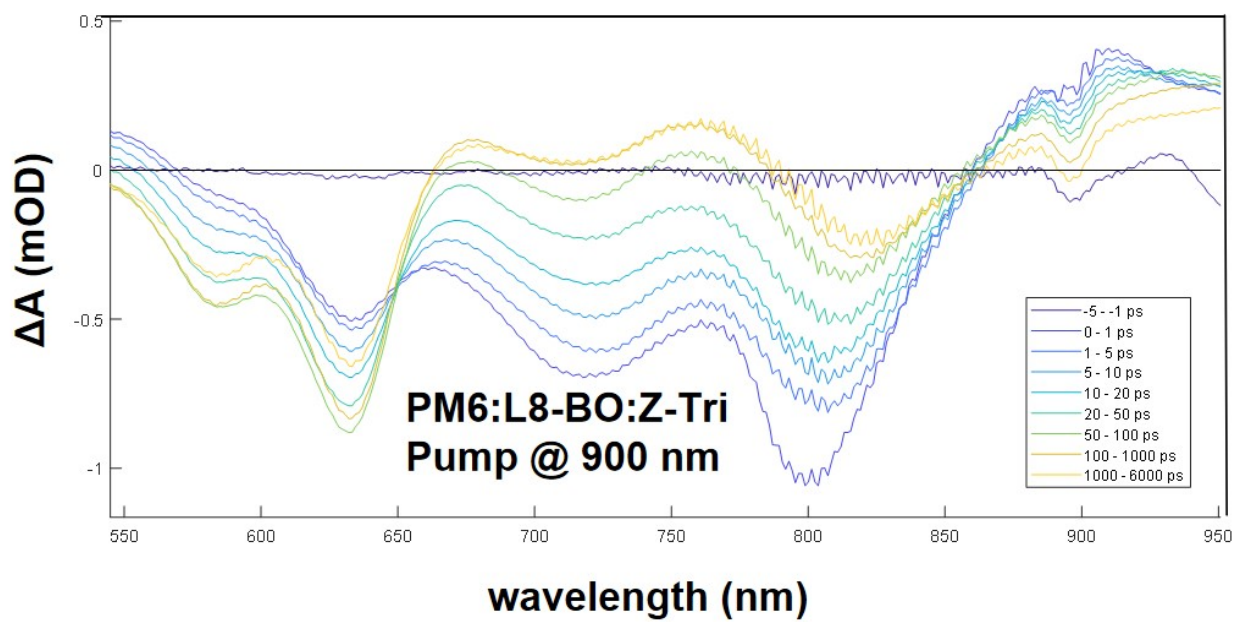


Fig. S20. TA spectra of the PM6:L8-BO:Z-Tri blends pumped at 900 nm.

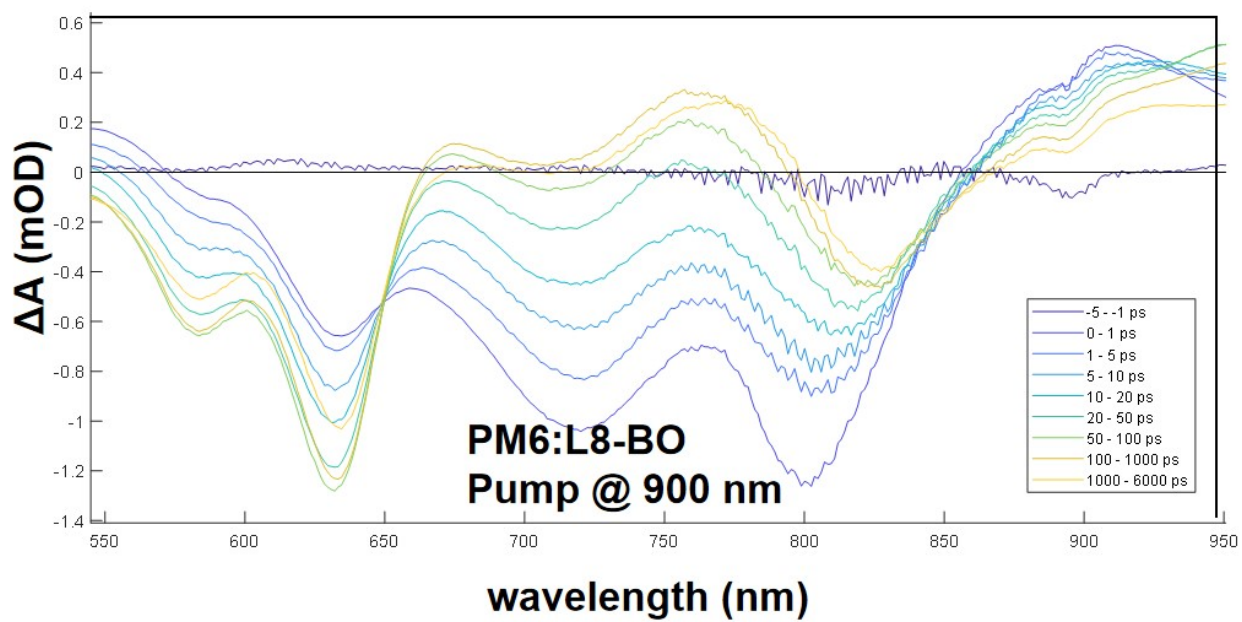


Fig. S21. TA spectra of the PM6:L8-BO blends pumped at 900 nm.

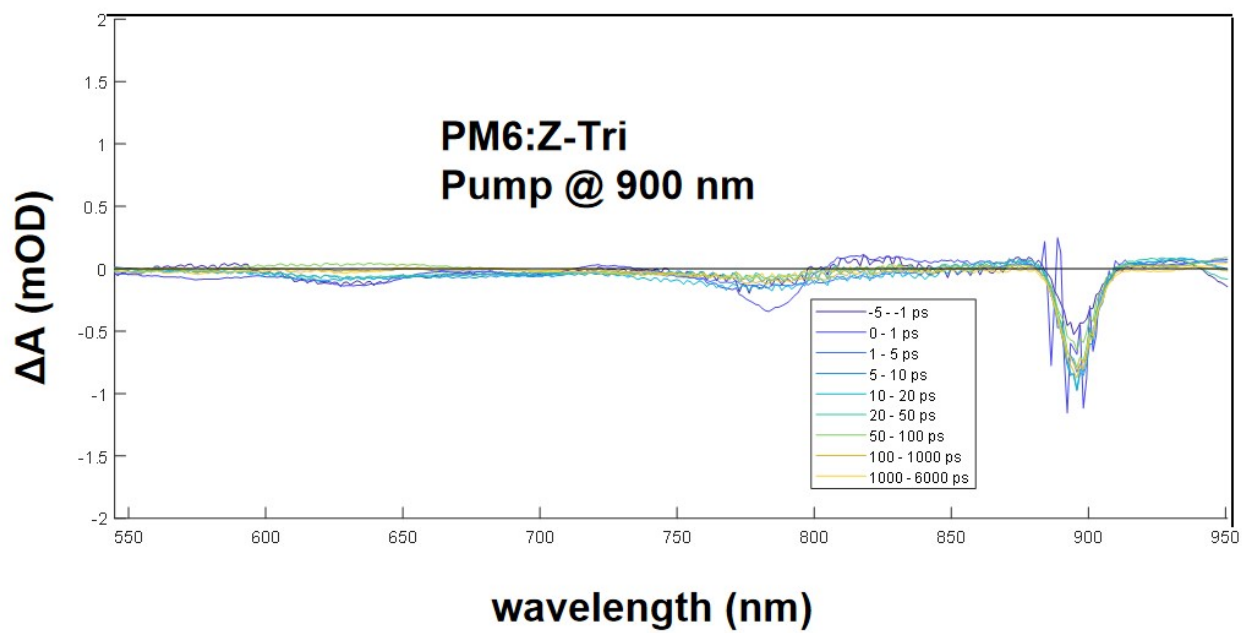


Fig. S22. TA spectra of the PM6:Z-Tri blends pumped at 900 nm.

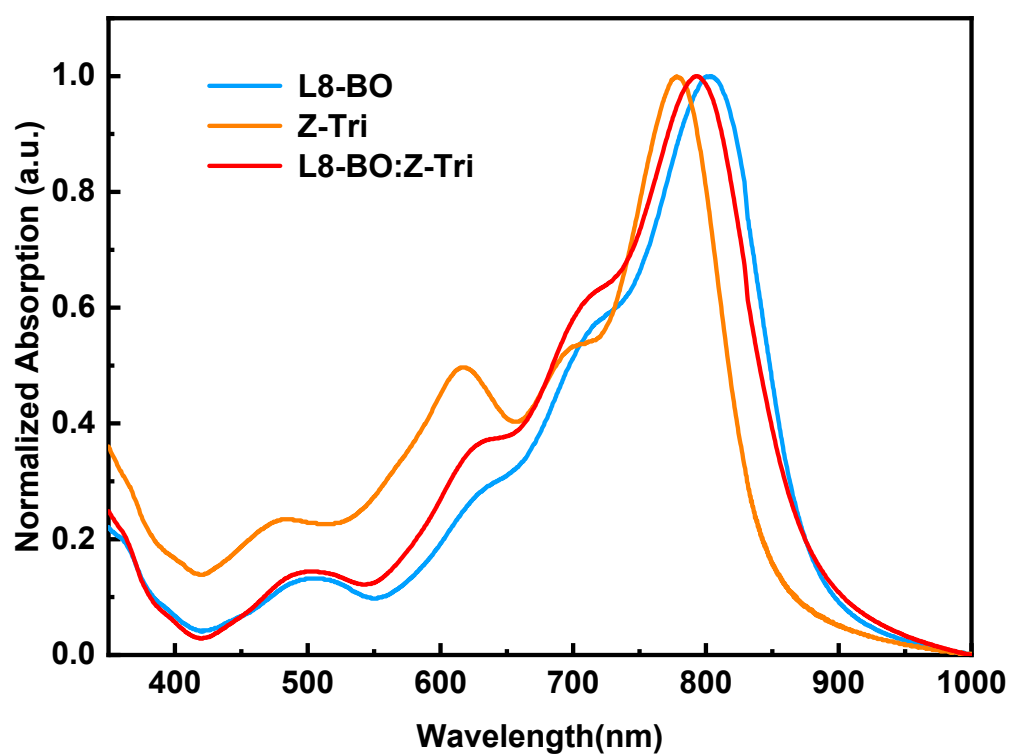


Fig. S23. UV-vis absorption spectra of L8-BO, Z-Tri, and L8-BO:Z-Tri.

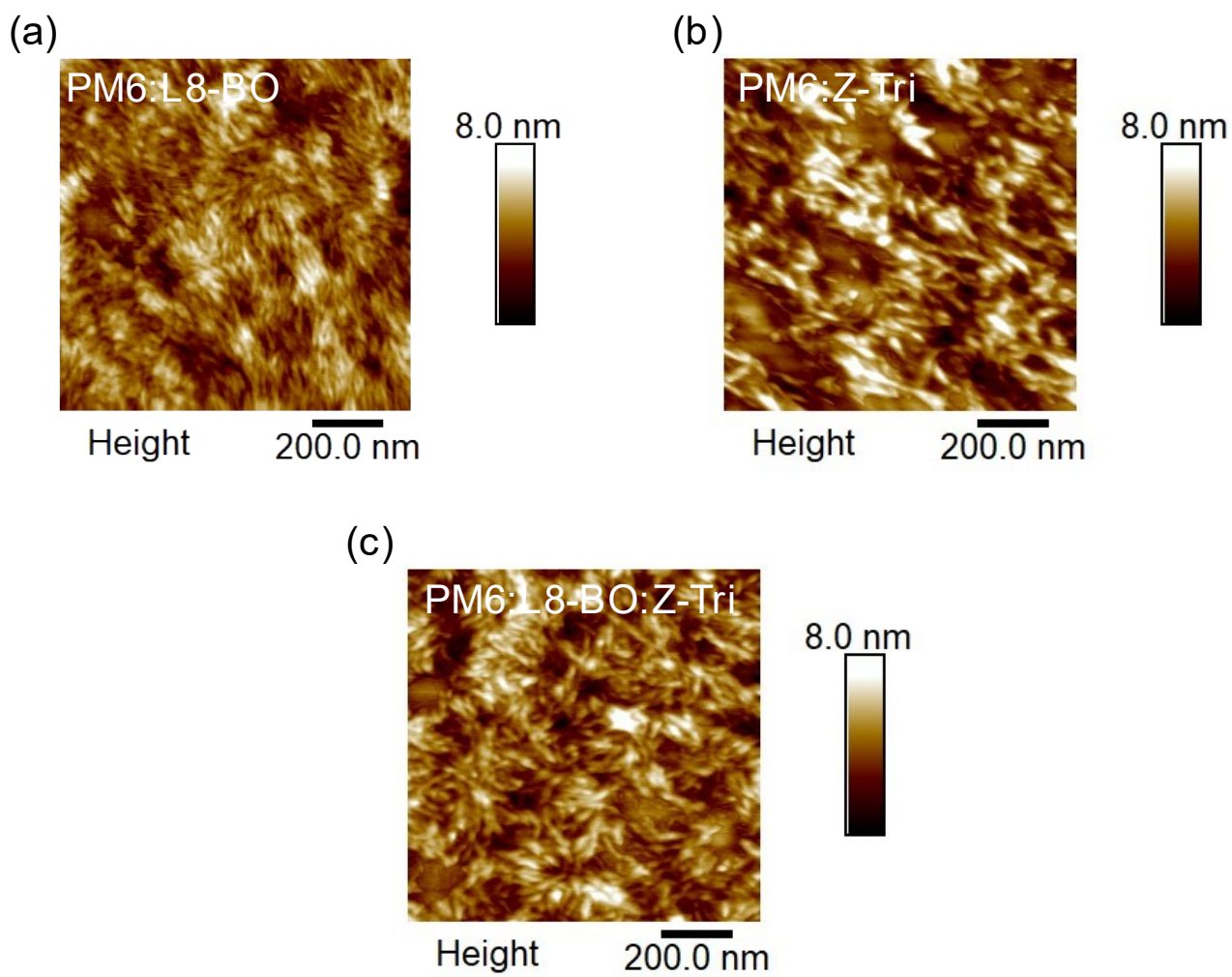


Fig. S24. AFM height images of (a) PM6:L8-BO, (b) PM6:Z-Tri, and (c) PM6:L8-BO:Z-Tri blend films.

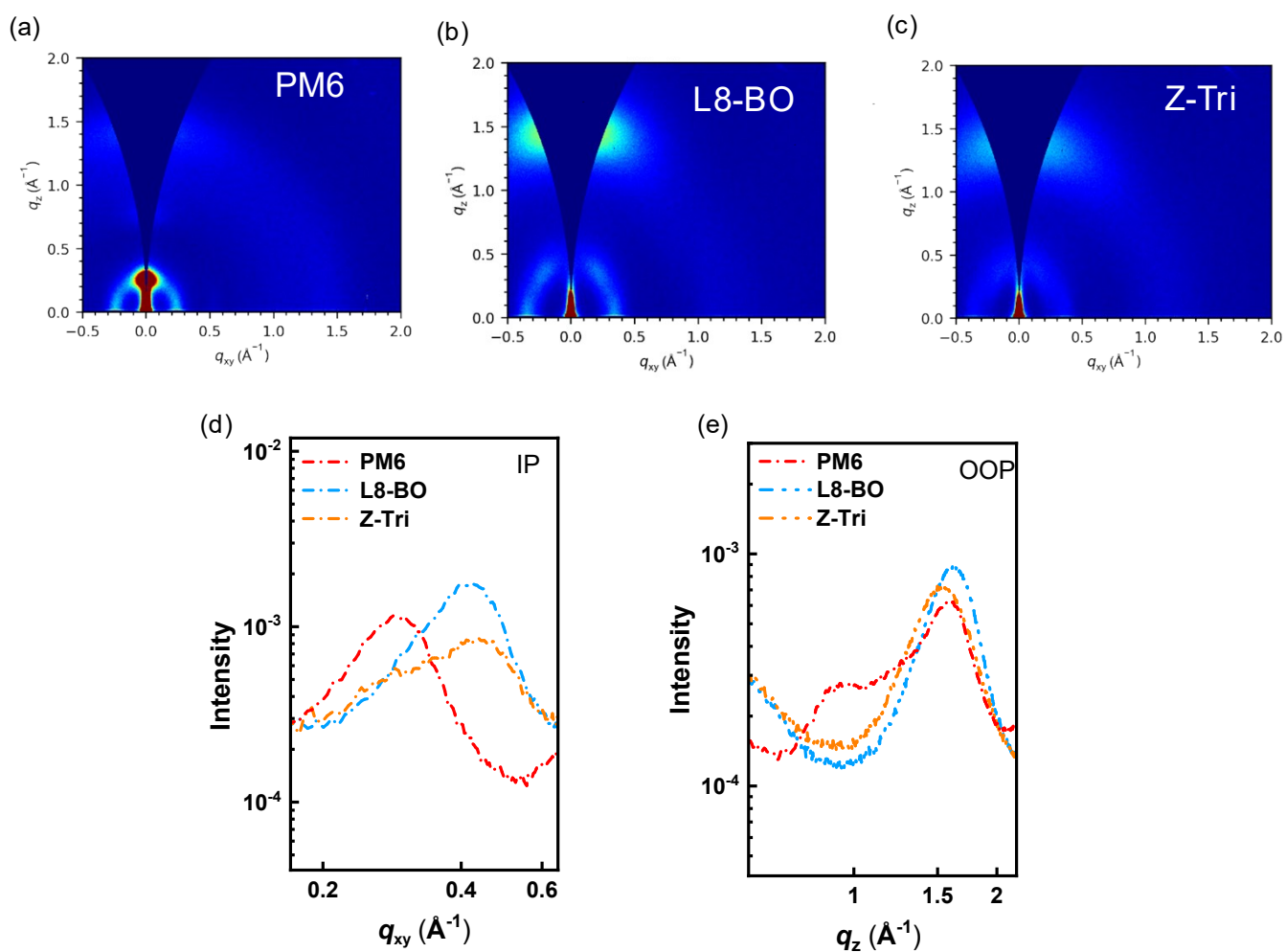


Fig. S25. The GIWAXS patterns of neat films of donor and acceptors. (a-c) The 2D GIWAXS patterns of the films; (d) In-plane and (e) out-of-plane cuts of the films with GIWAXS patterns.

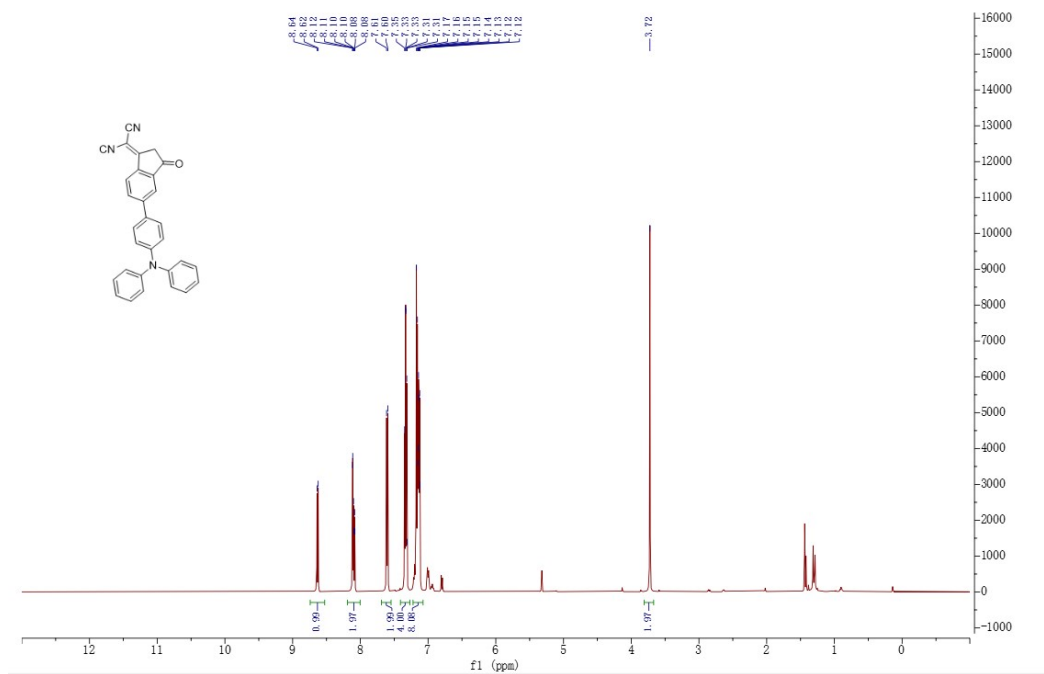


Fig. S26. ¹H-NMR spectrum of compound 3 in CD₂Cl₂.

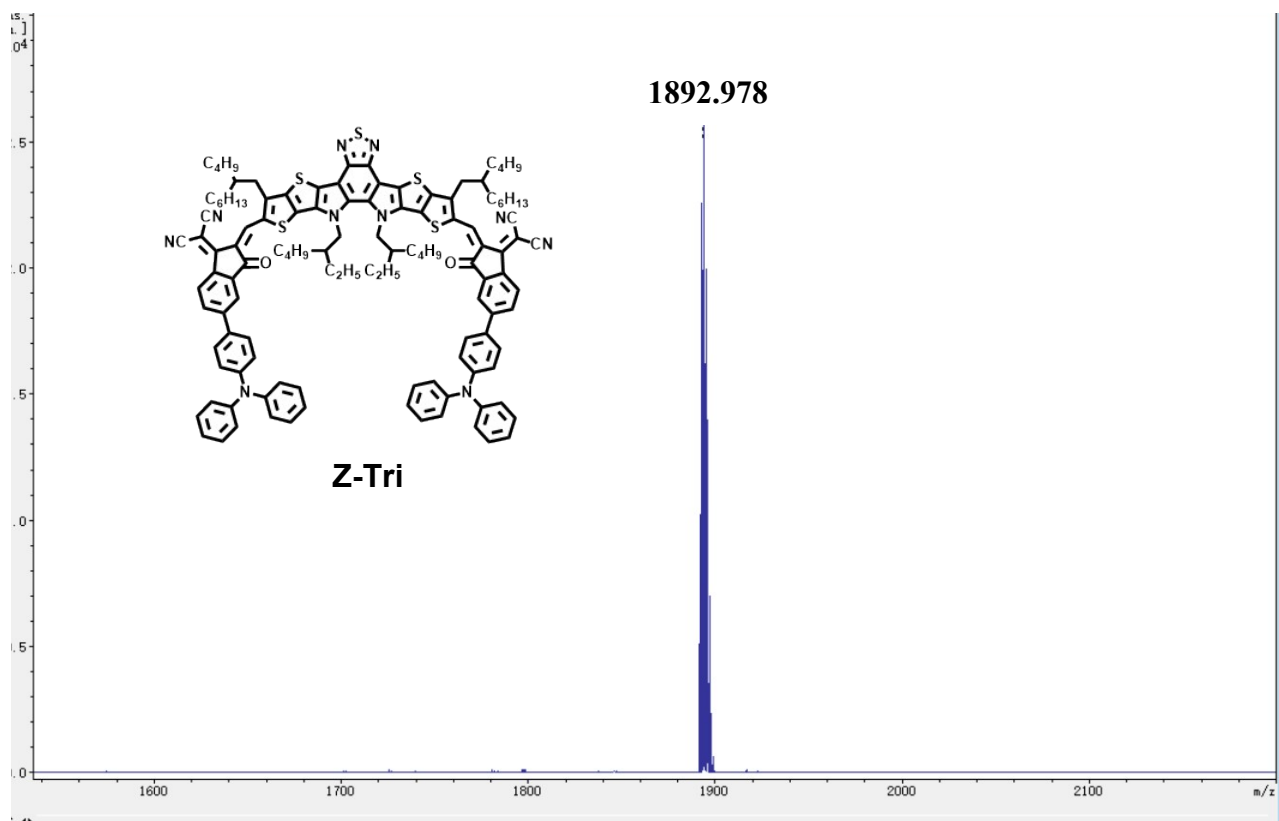


Fig. S27. MS (MALDI-TOF) spectrum of Z-Tri.

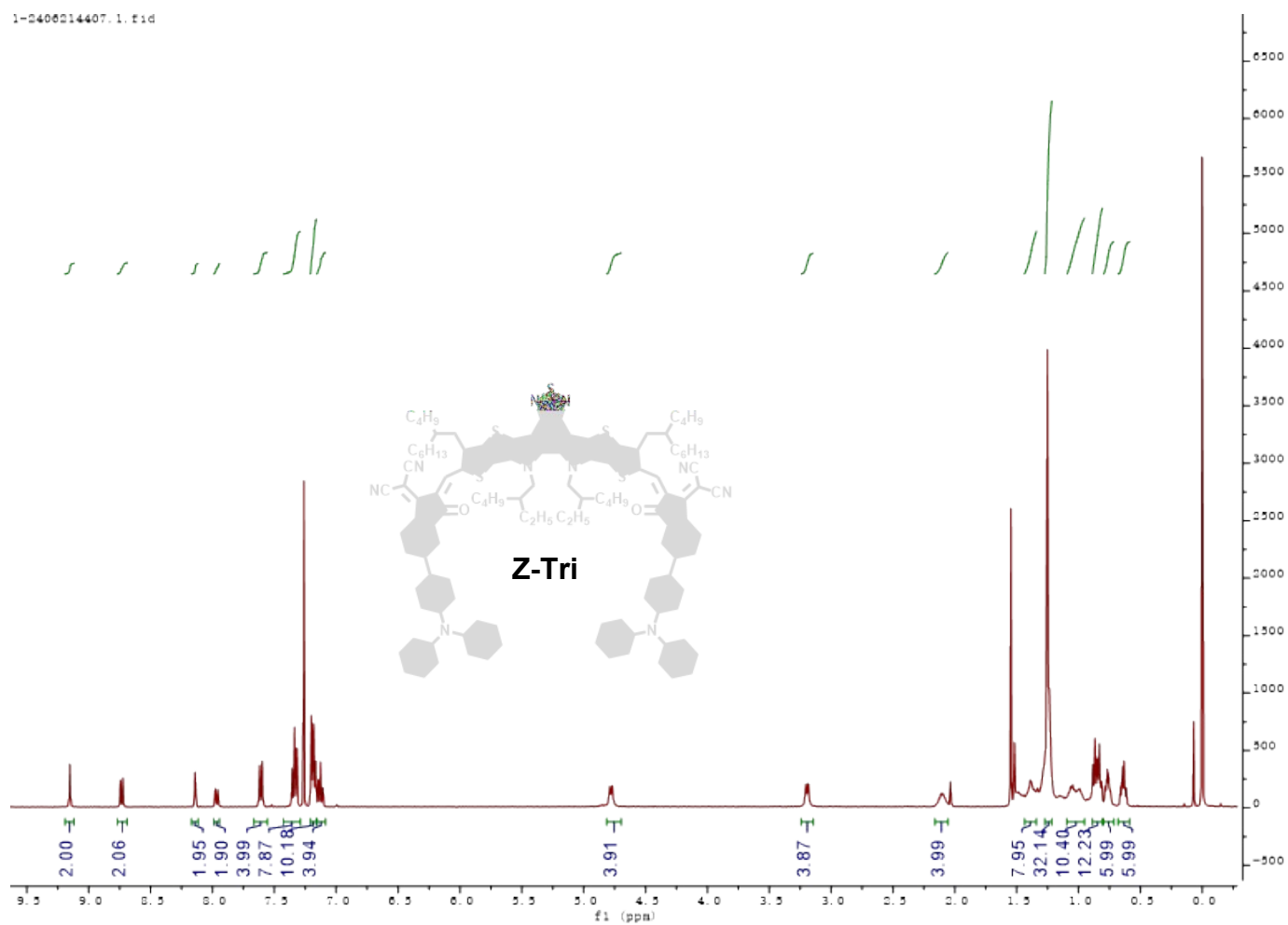


Fig. S28. ¹H-NMR spectrum of T Z-Tri in CDCl₃.

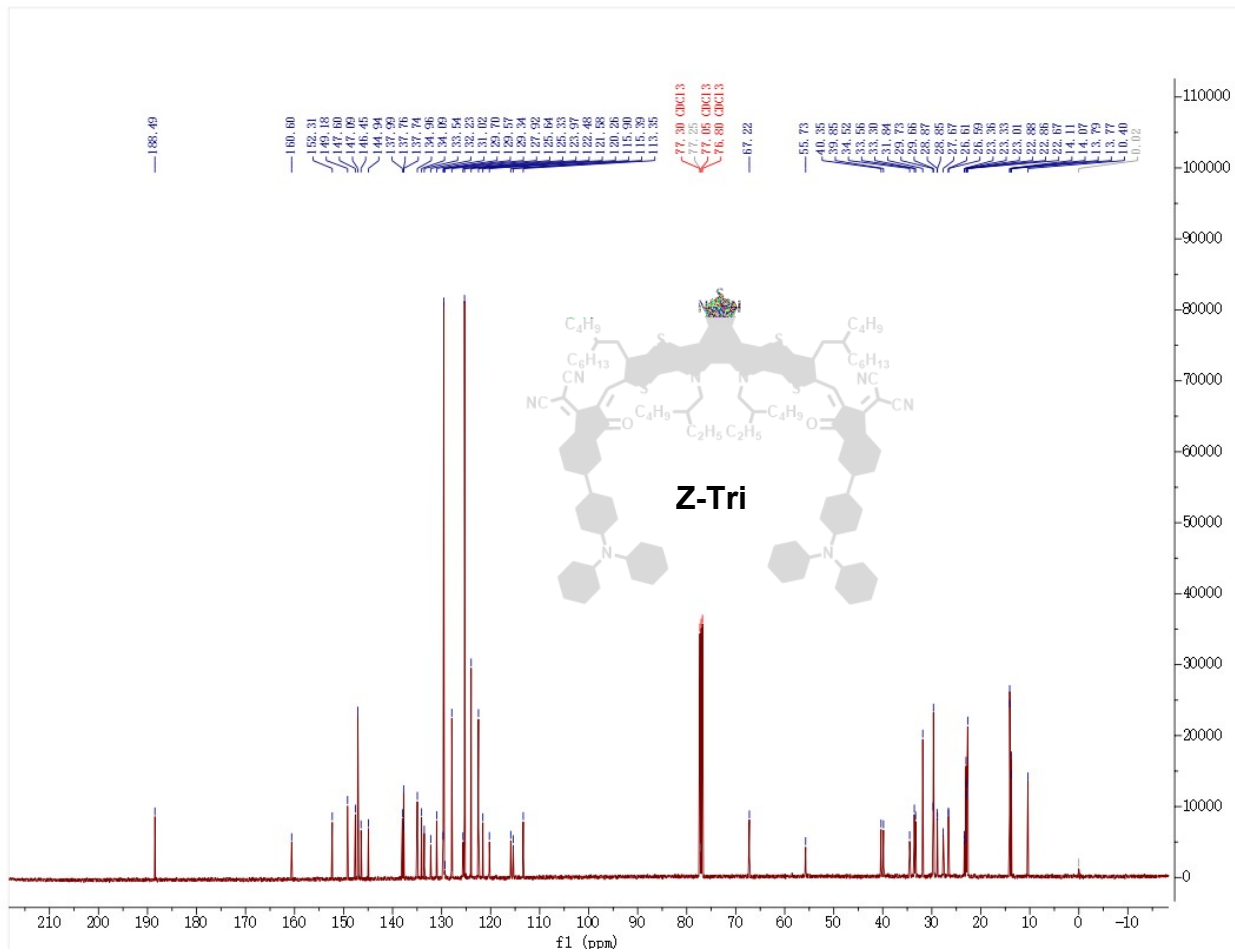


Fig. S29. ^{13}C -NMR spectrum of T Z-Tri in CDCl_3 .

Table S1. Optical and electrochemical properties of the photoactive materials.

Materials	$\lambda_{max}^{solution}$ a	λ_{max}^{film} b	λ_{onset}^{film} c	E_g^{opt} d	T_g e	E_{HOMO} f	E_{LUMO} g
	(nm)	(nm)	(nm)	(eV)	(°C)	(eV)	(eV)
L8-BO	728	805	885	1.40	106	-5.69	-3.88
Z-Tri	726	778	855	1.45	139	-5.45	-3.52

a) The maximum absorption in solutions; b) The maximum absorption in thin films; c) Absorption onsets in thin films; d) Optical band gap (E_g) was calculated through the onset of the thin-film absorption edge; e) Obtained by UV/Vis DMT results; f) Calculated by $E_{HOMO} = -4.80 \text{ eV} - E_{ox}$; g) $E_{LUMO} = -E_{red} - 4.80 \text{ eV}$.

Table S2. Summary of photovoltaic parameters of the ternary devices with different Z-Tri contents.

Active Layer	V_{oc} (V)	J_{sc} (mA cm ⁻²)	FF (%)	PCE (%) ^a
PM6:L8-BO (1:1.2)	0.894	26.51	80.1	18.98
PM6:L8-BO:Z-Tri (1:1.1:0.1)	0.901	26.83	80.0	19.34
PM6:L8-BO:Z-Tri (1:1:0.2)	0.927	27.30	80.3	20.32
PM6:L8-BO:Z-Tri (1:0.8:0.4)	0.948	20.17	75.0	14.34
PM6:L8-BO:Z-Tri (1:0.7:0.5)	0.950	19.98	69.2	13.13
PM6:L8-BO:Z-Tri (1:0.5:0.7)	0.954	17.99	59.8	10.26
PM6:L8-BO:Z-Tri (1:0.2:1)	0.958	15.62	47.5	7.11
PM6:Z-Tri (1:1.2)	1.001	9.22	43.0	3.97

a) Average values obtained from 30 devices.

Table S3. The hole mobilities and electron mobilities of the binary and ternary devices.

Active Layer	μ_h^a ($10^{-4} \text{ cm}^2 \text{ V}^{-1} \text{ s}^{-1}$)	μ_e^a ($10^{-4} \text{ cm}^2 \text{ V}^{-1} \text{ s}^{-1}$)	μ_h/μ_e
PM6:L8-BO	2.91 ± 0.35	2.34 ± 0.19	1.24
PM6:Z-Tri	2.68 ± 0.21	1.94 ± 0.14	1.38
PM6:L8-BO:Z-Tri	4.79 ± 0.15	4.21 ± 0.11	1.13

a) Average values obtained from 30 devices.

Table S4. Contact angle and surface tension data of PM6, L8-BO, and Z-Tri neat films.

Materials	θ_{water} (°)	θ_{glycerol} (°)	γ (mN m⁻¹)	χ
PM6	101.8	90.7	17.2	
L8-BO	92.7	78.4	26.1	0.93
Z-Tri	93.6	80.3	24.2	0.60

Table S5. Crystal coherence length and the d -spacings of (010) peaks in OOP direction and (100) peaks in IP direction of neat and blend films.

Materials	010 (OOP)				100 (IP)			
	q	d -spacing ^a	FWHM	CCL ^b	q	d -spacing ^a	FWHM	CCL ^b
	(\AA^{-1})	(\AA)	(\AA^{-1})	(\AA)	(\AA^{-1})	(\AA)	(\AA^{-1})	(\AA)
PM6	1.579	3.977	0.3794	14.73	0.288	21.80	0.1089	51.32
L8-BO	1.614	3.890	0.3821	14.63	0.409	15.35	0.1548	36.11
Z-Tri	1.530	4.104	0.4321	12.93	0.436	14.41	0.1911	29.25
PM6:L8-BO	1.618	3.881	0.3570	15.66	0.296	21.21	0.1021	54.74
PM6:Z-Tri	1.587	3.957	0.4162	13.43	0.308	20.38	0.0837	66.78
PM6:L8-BO:Z-Tri	1.621	3.874	0.3478	16.07	0.303	20.72	0.0929	60.16

a) Obtained by the equation of $d = 2\pi/q$, in which q corresponds to the diffraction peak positions; b)

Calculated using the equation: $CCL = 2\pi K/\text{FWHM}$, in which w is the full width at half maxima and K is a form factor (0.89 here).

Table S6. The photovoltaic performance for PM6:L8-BO:Z-Tri (1:1:0.2) based OSCs with different active layer thicknesses.

Thickness (nm)	V_{oc} (V)	J_{sc} (mA cm⁻²)	FF (%)	PCE (%)
100	0.929	26.88	78.7	19.65
110	0.928	26.98	79.1	19.80
120	0.927	27.30	80.3	20.32
130	0.917	27.01	79.7	19.74
140	0.911	26.97	79.7	19.58

Table S7. Summary of photovoltaic parameters for PM6:L8-BO:Z-Tri (1:1:0.2) devices with different annealing temperatures.

Temperature (°C)	V_{oc} (V)	J_{sc} (mA cm⁻²)	FF (%)	PCE (%)
80	0.928	26.49	79.1	19.44
100	0.927	27.30	80.3	20.32
120	0.924	26.85	79.3	19.67

Table S8. Comparison of efficiency and energy loss between this work and earlier references.

Active Layer	ΔE_{nr} (eV)	V_{oc} (V)	E_{loss} (eV)	PCE (%)	Ref.
PM6:CH17:F-2F	0.190	0.889	0.490	18.13	2
PM6:BTP-eC9:ZH2	0.241	0.862	0.514	18.75	3
D18:Y6:IDTT-SiO-IC	0.212	0.896	0.531	18.77	4
PM6:CH-ThCl:CH-6F	0.208	0.932	0.508	18.80	5
PM6:L8-BO:BTP-S9	0.189	0.872	0.540	18.84	6
PBQx-TF:eC9-2Cl:F-BTA3	0.219	0.879	0.551	19.00	7
PM1:L8-BO:BTP-F3Cl	0.186	0.885	0.549	19.10	8
D18:Aqx-18:L8-BO	0.198	0.928	0.543	19.10	9
PM1:L8-BO:BTP-2F2Cl	0.197	0.881	0.547	19.17	10
PM6:L8-BO:BTP-H2	0.196	0.892	0.558	19.20	11
PM6:D18-Cl:L8-BO	0.208	0.910	0.546	19.22	12
PM6:L8-BO-X:Tri-V	0.212	0.892	0.539	19.86	13
PM6:BTP-eC9:o-BTP-eC9	0.190	0.860	0.525	19.88	14
PM6:BO-4Cl:BO-5Cl	0.198	0.872	0.498	18.56	15
PNTB-2T:Y6:PC71BM	0.217	0.875	0.533	17.35	16
PM6:BTP-4F-12:MeIC	0.227	0.863	0.526	17.40	17
PM6:Y6:S3	0.223	0.856	0.579	17.53	18
PM6:Y6:C8-DTC	0.215	0.873	0.537	17.52	19
PM6:Y6:3TP3T-4F	0.220	0.85	0.560	16.70	20
PM6:BTP-eC9:L8-BO-F	0.199	0.853	0.519	18.66	21

PM6:Y6:ZY-4Cl	0.198	0.863	0.520	18.69	22
PM6:L8-BO-X:Y-C10ch	0.223	0.886	0.544	19.10	23
PM6:BTP-eC9:PhC6-IC-F	0.140	0.835	0.545	18.33	24
PM6:BTP-eC9:5BDDBDT-Cl	0.220	0.854	0.540	18.43	25
D18:N3-BO:F-BTA3	0.183	0.924	0.534	20.25	26
PM6:PY-1S1Se:PY-2Cl	0.184	0.914	0.523	18.20	27
PM6:IDTR:L8-BO	0.234	0.902	0.550	19.12	28
PM6:BTP-BO4Cl:5BDTBDD	0.224	0.843	0.545	17.54	29
PM6:BTP-eC9:MOIT-M	0.210	0.87	0.520	18.50	30
D18:Z8:L8-BO	0.190	0.92	0.510	20.20	31
D18:BTP-eC9-4F:DM-F	0.180	0.89	0.540	19.49	32
PM6:L8-BO:Z-Tri	0.196	0.927	0.571	20.32	This work

3. References

1. C. Li, J. Zhou, J. Song, J. Xu, H. Zhang, X. Zhang, J. Guo, L. Zhu, D. Wei, G. Han, J. Min, Y. Zhang, Z. Xie, Y. Yi, H. Yan, F. Gao, F. Liu and Y. Sun, *Nat. Energy*, 2021, **6**, 605-613.
2. H. Chen, Y. Zou, H. Liang, T. He, X. Xu, Y. Zhang, Z. Ma, J. Wang, M. Zhang, Q. Li, C. Li, G. Long, X. Wan, Z. Yao and Y. Chen, *Sci. China Chem.*, 2022, **65**, 1362-1373.
3. Y. Zhang, J. Deng, S. You, X. Huang, J. Liu, Y. Cheng, B. Huang, X. Chen, Z. Sun, C. Yang, Q. Y. Cao, F. Wu and L. Chen, *Adv. Funct. Mater.*, 2023, **34**.
4. F. Meng, Y. Qin, Y. Zheng, Z. Zhao, Y. Sun, Y. Yang, K. Gao and D. Zhao, *Angew. Chem. Int. Ed.*, 2023, **62**, e202217173.
5. X. Si, Y. Huang, W. Shi, R. Wang, K. Ma, Y. Zhang, S. Wu, Z. Yao, C. Li, X. Wan and Y. Chen, *Adv. Funct. Mater.*, 2023, **33**, 2306471.
6. C. He, Q. Shen, B. Wu, Y. Gao, S. Li, J. Min, W. Ma, L. Zuo and H. Chen, *Adv. Energy Mater.*, 2023, **13**, 2204154.

7. Y. Cui, Y. Xu, H. Yao, P. Bi, L. Hong, J. Zhang, Y. Zu, T. Zhang, J. Qin, J. Ren, Z. Chen, C. He, X. Hao, Z. Wei and J. Hou, *Adv. Mater.*, 2021, **33**, 2102420.
8. J. Wan, Y. Wu, R. Sun, J. Qiao, X. Hao and J. Min, *Energy Environ. Sci.*, 2022, **15**, 5192-5201.
9. K. Liu, Y. Jiang, F. Liu, G. Ran, F. Huang, W. Wang, W. Zhang, C. Zhang, J. Hou and X. Zhu, *Adv. Mater.*, 2023, **35**, 2300363.
10. R. Sun, Y. Wu, X. Yang, Y. Gao, Z. Chen, K. Li, J. Qiao, T. Wang, J. Guo, C. Liu, X. Hao, H. Zhu and J. Min, *Adv. Mater.*, 2022, **34**, 2110147.
11. C. He, Y. Pan, Y. Ouyang, Q. Shen, Y. Gao, K. Yan, J. Fang, Y. Chen, C.-Q. Ma, J. Min, C. Zhang, L. Zuo and H. Chen, *Energy Environ. Sci.*, 2022, **15**, 2537-2544.
12. J. Gao, N. Yu, Z. Chen, Y. Wei, C. Li, T. Liu, X. Gu, J. Zhang, Z. Wei, Z. Tang, X. Hao, F. Zhang, X. Zhang and H. Huang, *Adv. Sci.*, 2022, **9**, 2203606.
13. J. Song, C. Zhang, C. Li, J. Qiao, J. Yu, J. Gao, X. Wang, X. Hao, Z. Tang, G. Lu, R. Yang, H. Yan and Y. Sun, *Angew. Chem. Int. Ed.*, 2024, **63**, e202404297.
14. J. Fu, Q. Yang, P. Huang, S. Chung, K. Cho, Z. Kan, H. Liu, X. Lu, Y. Lang, H. Lai, F. He, P. W. K. Fong, S. Lu, Y. Yang, Z. Xiao and G. Li, *Nat. Commun.*, 2024, **15**, 1830.
15. C. He, Z. Chen, T. Wang, Z. Shen, Y. Li, J. Zhou, J. Yu, H. Fang, Y. Li, S. Li, X. Lu, W. Ma, F. Gao, Z. Xie, V. Coropceanu, H. Zhu, J.-L. Bredas, L. Zuo and H. Chen, *Nat. Commun.*, 2022, **13**, 2598.
16. G. Zhang, H. Ning, H. Chen, Q. Jiang, J. Jiang, P. Han, L. Dang, M. Xu, M. Shao, F. He and Q. Wu, *Joule*, 2021, **5**, 931-944.
17. X. Ma, J. Wang, J. Gao, Z. Hu, C. Xu, X. Zhang and F. Zhang, *Adv. Energy Mater.*, 2020, **10**, 2001404.
18. Q. An, J. Wang, X. Ma, J. Gao, Z. Hu, B. Liu, H. Sun, X. Guo, X. Zhang and F. Zhang, *Energy Environ. Sci.*, 2020, **13**, 5039-5047.
19. Q. Ma, Z. Jia, L. Meng, J. Zhang, H. Zhang, W. Huang, J. Yuan, F. Gao, Y. Wan, Z. Zhang and Y. Li, *Nano Energy*, 2020, **78**, 105272.

20. J. Song, C. Li, L. Zhu, J. Guo, J. Xu, X. Zhang, K. Weng, K. Zhang, J. Min, X. Hao, Y. Zhang, F. Liu and Y. Sun, *Adv. Mater.*, 2019, **31**, 1905645.
21. Y. Cai, Y. Li, R. Wang, H. Wu, Z. Chen, J. Zhang, Z. Ma, X. Hao, Y. Zhao, C. Zhang, F. Huang and Y. Sun, *Adv. Mater.*, 2021, **33**, 2101733.
22. X. Duan, W. Song, J. Qiao, X. Li, Y. Cai, H. Wu, J. Zhang, X. Hao, Z. Tang, Z. Ge, F. Huang and Y. Sun, *Energy Environ. Sci.*, 2022, **15**, 1563-1572.
23. C. Xiao, X. Wang, T. Zhong, R. Zhou, X. Zheng, Y. Liu, T. Hu, Y. Luo, F. Sun, B. Xiao, Z. Liu, C. Yang and R. Yang, *Adv. Sci.*, 2023, **10**, 2206580.
24. D. Sun, Z. Chen, J. Zhang, W. Song, J. Shi, J. Zhu, Y. Meng, F. Jin, S. Yang and Z. Ge, *Sci. China Chem.*, 2023, **67**, 963-972.
25. H. Xia, Y. Zhang, K. Liu, W. Deng, M. Zhu, H. Tan, P. W. K. Fong, H. Liu, X. Xia, M. Zhang, T. A. Dela Peña, R. Ma, M. Li, J. Wu, Y. Lang, J. Fu, W.-Y. Wong, X. Lu, W. Zhu and G. Li, *Energy Environ. Sci.*, 2023, **16**, 6078-6093.
26. C. Li, G. Yao, X. Gu, J. Lv, Y. Hou, Q. Lin, N. Yu, M. S. Abbasi, X. Zhang, J. Zhang, Z. Tang, Q. Peng, C. Zhang, Y. Cai and H. Huang, *Nat. Commun.*, 2024, **15**, 8872.
27. R. Sun, T. Wang, Q. Fan, M. Wu, X. Yang, X. Wu, Y. Yu, X. Xia, F. Cui, J. Wan, X. Lu, X. Hao, A. K. Y. Jen, E. Spiecker and J. Min, *Joule*, 2023, **7**, 221-237.
28. C. Zhang, X. Zhong, X. Sun, Y. Wei, H. Wang, F. Wang, Y. Ji, X. Ding, J. Lv, S. Pang, H. Hu, K. Wang and M. Xiao, *Chem. Eng. J.*, 2025, **504**, 158530.
29. H. Xia, Y. Zhang, W. Deng, K. Liu, X. Xia, C. J. Su, U. S. Jeng, M. Zhang, J. Huang, J. Huang, C. Yan, W. Y. Wong, X. Lu, W. Zhu and G. Li, *Adv. Mater.*, 2022, **34**, 2107659.
30. X. Yan, J. Wu, J. Lv, L. Zhang, R. Zhang, X. Guo and M. Zhang, *J. Mater. Chem. A*, 2022, **10**, 15605-15613.
31. Y. Jiang, S. Sun, R. Xu, F. Liu, X. Miao, G. Ran, K. Liu, Y. Yi, W. Zhang and X. Zhu, *Nat. Energy*, 2024, **9**, 975-986.
32. H. Lu, D. Li, W. Liu, G. Ran, H. Wu, N. Wei, Z. Tang, Y. Liu, W. Zhang and Z. Bo, *Angew.*

